Copyright © 2025 Elsevier Ltd. All rights reserved. This manuscript version is made available under the CC-BY-NC-ND 4.0 license
https://creativecommons.org/licenses/by-nc-nd/4.0/ (see: https://www.elsevier.com/about/policies/sharing).

Inverse Machine Learning for the Design of Perforated Beams: Parent Section and Material Prediction

Sina Sarfarazi[a], Rabee Shamass[b], Musab Rabi[c], Ikram Abarkan[d], Felipe Piana Vendramell Ferreira[e], Konstantinos Daniel Tsavdaridis[f]

[a] Department of Structures for Engineering and Architecture, University of Naples "Federico II," Naples 80125, Italy
[b] Department of Civil and Environmental Engineering, Brunel University London, London, UB8 3PH, UK
[c] Department of Civil Engineering, Jerash University, 26150, Jordan
[d] Department of Physics, Faculty of Sciences, Abdelmalek Essaâdi University, 93002, Tetouan, Morocco
[e] Department of Civil Engineering, State University of Maringa, Maringa, Parana, Brazil
[f] Department of Engineering, School of Science and Technology, City, University of London, Northampton Square, London, EC1V 0HB, United Kingdom

Abstract

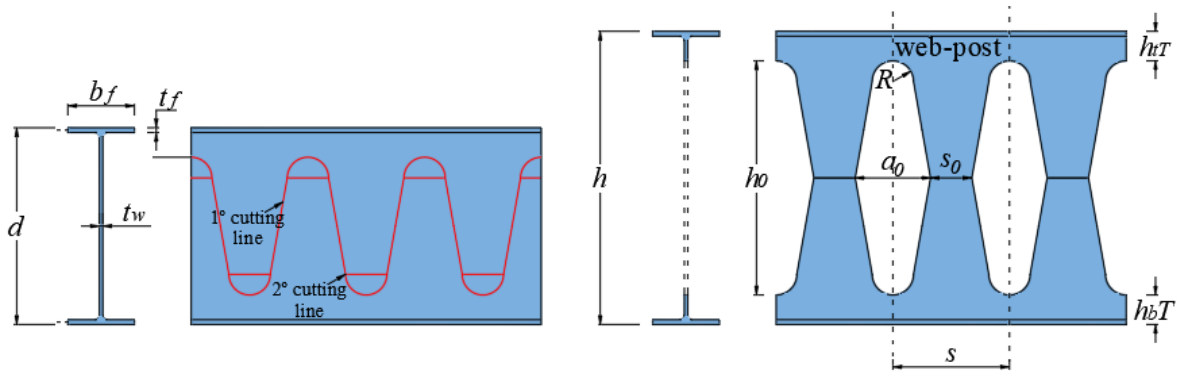
This study introduces a novel machine learning-based inverse design methodology for predicting the parent cross-sectional and material properties of perforated steel beams with elliptically-based openings. Unlike conventional forward design or optimization-based methods, the proposed approach frames structural design as an inverse problem. It enables the direct mapping of opening geometry and resistance parameters to essential properties such as section depth, flange width, web thickness, flange thickness, and yield strength. Five advanced supervised machine learning models— Histogram-Based Gradient Boosting, Random Forest, Extreme Gradient Boosting, k-Nearest Neighbours, and Support Vector Regression—were trained on a dataset generated through forward structural analysis. This methodology develops non-iterative surrogate models that enhance the generalizability and accessibility of the structural design process. The models demonstrated excellent predictive performance, with coefficient of determination (R^2) values exceeding 0.99 for most outputs. Shapley Additive Explanations (SHAP) analysis identified web-post buckling resistance and section height as the most influential input features, with other variables contributing depending on the output. The proposed inverse learning framework was also benchmarked against an analytical design model to assess accuracy and consistency. To support practical implementation, a user-friendly web tool was developed, allowing engineers and researchers to access instant prediction. Overall, this research offers an efficient and explainable data-driven solution for structural design, demonstrating the practical value of artificial intelligence in engineering applications.

Keywords: Inverse Structural Design; Explainable Artificial Intelligence; Surrogate Modelling; Structural Design Automation; Perforated Steel Beams

1. Introduction

Steel beams with elliptically-based web openings are fabricated through the castellation process, which involves cutting and welding of the parent section to create an expanded beam section [1], as shown in Fig. 1. Widely used in construction, these beams offer benefits such as enhanced flexural stiffness, reduced self-weight, and lower structural floor heights. The web openings (often circular, hexagonal, square and elongated rectangular) allow for the integration of hydraulic and electrical systems within the beam, removing the need for external installations. However, perforated beams

exhibit complex structural behaviours and are prone to failure modes, including plasticisation from Vierendeel bending and various buckling modes [2]. The present study focuses on web-post buckling (WPB), a local phenomenon characterised by lateral displacement and torsion due to horizontal shear [3], as these particular design of perforated steel beams with elliptically-based web openings over-perform under high vertical shear forces and Vierendeel bending, which make web-post to be the most common failure mode. Key factors affecting WPB resistance include web opening height, web-post width (or opening spacing), and web thickness [4].



(a) (b)

Fig. 1: Geometry of steel beams with elliptically-based web openings: (a) castellation process and geometric descriptors of the parent section, (b) resulting perforated beam with key parameters of the web-post region, adapted from [1]

Researchers [5–7] investigated various web opening shapes and found that elliptically-based web openings offer better resistance to plasticisation and lower additional deflections at the centreline of the web-opening due to high capacity in Vierendeel bending actions. Three-point bending tests showed that steel beams with elliptically-based web openings had higher WPB resistance [8]. Studies using finite element (FE) models [1] and Artificial Neural Networks (ANN) [9] demonstrated that steel profile geometries, such as height and web thickness, positively affect WPB capacity, while elliptically-based web openings dimensions (i.e., openings height, width and radius) had a negative impact. Despite some analytical models and high-strength steel studies [10], machine learning (ML) methods have also been used to predict WPB capacity and evaluate design models [11]. The ML models used for the steel beams with elliptically-based web openings employ the geometric characteristics of the steel profile and material strength as input, with the output being the capacity under specific failure modes. Recent studies have demonstrated the growing role of computational intelligence in engineering optimisation. Ghorbany et al. [12] applied chaotic multi-objective optimisation to improve vehicle suspension. Wang et al. [13] explored topology optimisation in active tensegrity structures. Li et al. [14] used deep learning for fatigue crack detection, while Khosravian et al. [15]

developed AI-based real-time vehicle control. Xu et al. [16] reviewed data-driven methods for designing functional coatings. Momen et al. [17] optimised piezoelectric energy harvesters using evolutionary algorithms, and Chen et al. [18] introduced a Bayesian surrogate model for stochastic structural updating. Together, these works reflect the broader adoption of machine learning, optimisation, and inverse analysis across structural, mechanical, and materials engineering domains. Recent studies have also proposed simplified design-oriented characterizations to reduce reliance on full-scale nonlinear analysis [19,20]. However, the use of inverse design for optimising structural design based on geometric and mechanical properties has not been studied yet.

Inverse Machine Learning (IML) has been utilised for its capacity to quickly investigate complex geometrical patterns in structural design on a large scale [21]. It provides an effective method for exploring complex geometrical patterns. In structural engineering, the design process typically requires multiple iterations, which can be costly for complex systems [22]. A key challenge of inverse problems is that they are often ill-posed, lacking unique or stable solutions, and consequently, various methods have been developed to solve these problems [23,24]. It is especially effective in addressing metamaterials and advanced structural systems where the relationships between geometry, material properties, and performance are highly nonlinear and complex. This technique is versatile and suitable for designing and optimising various metamaterials, including those aimed at impact absorption, improved deformation or buckling strengths, and shape recovery [25]. Although the models adopted in the current study are conventional supervised learners, the term IML reflects the inversion of the learning task: the inputs are structural performance targets and geometric descriptors of the web opening, while the predicted outputs are parent beam dimensions and material properties. This contrasts with typical forward ML approaches that predict performance based on known section data. The term is used to emphasise that the model is not used for analysis, but for design — effectively bypassing traditional iterative search or simulation-based workflows. This perspective has motivated a growing body of inverse design research across diverse engineering disciplines. For instance, Masurkar et al. [22] developed a ML model to infer elastic constants of orthotropic composites from time-series data. Teimouri et al. [25] proposed an inverse framework to optimise plate-lattice structures with tailored compressive strength. McClarren et al. [26] applied deep neural networks to infer hohlraum geometry and laser pulse profiles from experimental diagnostics. Islam et al. [27] integrated inverse optimisation into automated fibre placement systems to enhance composite manufacturing quality. Other works have addressed inverse prediction of hardness in multilayer coatings [28], and data-driven design of cellular structures with custom properties [29].

This study proposes a novel inverse design framework to predict parent beam section and material properties, including section depth (d), flange width (b_f), flange thickness (t_f), web thickness (t_w), and yield strength (f_y), based on design requirements. The methodology employs five supervised ML models including Histogram-Based Gradient Boosting (HistGB), Random Forest (RF), Extreme Gradient Boosting (XGB), k-Nearest Neighbours (KNN), and Support Vector Regression (SVR) trained on a systematically generated FEM dataset. Input features include key geometric and resistance parameters such as WPB resistance, web opening height (h_o), opening width (a_o), total beam height (h), and opening spacing (s). To ensure model transparency, SHapley Additive exPlanations (SHAP) analysis is applied, highlighting the influence of each feature on model outputs. Model performance is further validated against the analytical approach of Ferreira et al. [1]. A web-based design tool has also been developed to provide engineers with instant prediction and visualization of section and material properties. Fig. 2 provides a graphical summary of the proposed framework.

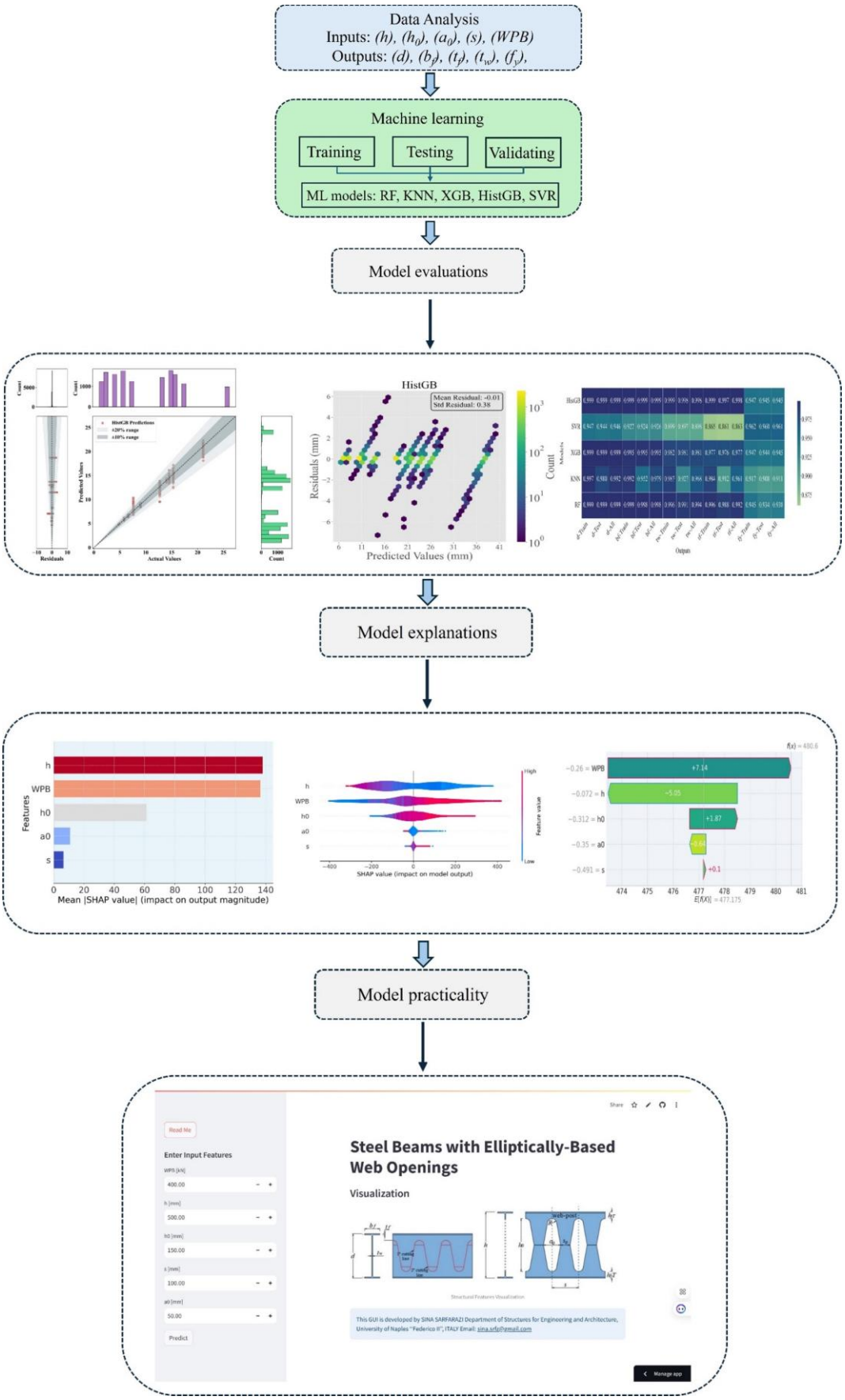


Fig. 2: Graphical summary of the proposed methodology for perforated beam design.

2. Research Significance

In recent years, the scientific community has prioritised reducing structural costs through optimised material, fabrication, and maintenance. Efforts focus on minimising material use [30] while meeting safety standards [31], with cutting losses from trimming steel lengths identified as a major source of waste [32]. In the case of steel beams with elliptically-based web openings, the cutting process is presented in GB 2492176 [33].

The design verification and resistance calculations for steel beams with web openings are addressed in Steel Design Guide 31 [34] (circular and hexagonal openings), SCI P355 [35] (rectangular and circular openings), and more recently, BS EN 1993-1-13 [36] (rectangular, circular, elongated, hexagonal, and sinusoidal openings). These standards consider various failure modes, including global bending, shear, Vierendeel bending of the tees, web-post shear, and web-post buckling. However, none of them address steel beams with elliptically-based web openings.

Motivated by these practical inefficiencies, this study introduces an IML framework for the design of perforated steel beams. The novelty of this approach lies in its ability to directly link desired structural outcomes, with a specific focus on web-post buckling (WPB) resistance, to design parameters such as parent section dimensions and material properties. WPB was selected because it is the most common and critical failure mode in beams with elliptically-based web openings, while other modes (e.g., global bending or shear) are already well addressed in existing design guides [1, 5-11]. Unlike conventional forward design methods, which begin with section and material properties and then predict performance through iterative FE analyses or analytical models, the proposed framework inverts this logic: it allows designers to start from performance requirements and directly obtain the necessary section and material properties. This eliminates costly trial-and-error refinements, reduces computational effort, and enables the discovery of non-intuitive yet high-performing solutions. To the best of the authors' knowledge, this is the first IML model developed specifically for perforated steel beams with elliptically-based web openings, and also the first to include yield strength (material grade) as a target prediction, extending inverse structural design beyond geometry to material classification.

This work also incorporates explainable AI (SHAP analysis) to provide insight into the relative influence of geometric and resistance parameters on each output, making the model interpretable and trustworthy. In addition, the inverse ML model is evaluated against analytical solutions derived from Eurocode 3-based design models, confirming both accuracy and practical relevance. To further support practical implementation, a user-friendly web application is developed, enabling designers and

researchers to quickly obtain optimized design parameters and incorporate them into real-world projects. This tool enhances the accessibility of the model, ensuring its relevance and applicability to industry professionals.

3. Data Analysis

3.1. FEM development

The validation study comprises two main stages. First, full FE models are developed based on the experimental work of Tsavdaridis and D'Mello [8]. In the second stage, simplified single web-post models are created to enable focused analysis of key parameters affecting buckling resistance—such as web-post width and web opening height. This approach is widely adopted in the literature [1].

All simulations are performed using ABAQUS [37]. A geometrically and materially nonlinear analysis with imperfections (GMNIA) is employed, following methodologies used by researchers studying steel beams with regular web openings [38]. An imperfection amplitude of $h/500$ is adopted, as recommended by Panedpojaman et al. [39], to account for manufacturing-induced deviations.

Material properties correspond to S355 steel, with a Young's modulus of 200 GPa and Poisson's ratio of 0.3. A multi-linear stress–strain relationship is applied, consistent with the model used by Shamass and Guarracino [40]. A mesh size of 10 mm is selected based on sensitivity studies by Ferreira et al. [41,42]. The structural components are modelled using S4R shell elements, which allow for six degrees of freedom and ensure computational efficiency with accurate results. For boundary conditions in the full models, vertical and longitudinal displacements are restricted at one stiffener end ($U_y = U_z = 0$), while only vertical movement is restrained at the other ($U_y = 0$). Lateral displacement and rotation around the longitudinal axis ($U_x = UR_z = 0$) are restrained at both ends near the stiffeners. In the web-post models, one end of the tee sections is fully fixed ($U_x = U_y = U_z = 0$), while the opposite end has restricted lateral displacement and rotations at both flanges ($U_x = UR_y = UR_z = 0$) and webs ($U_x = UR_x = UR_y = 0$). A shell edge load is applied along the web on the right-hand side of the model. The validation results are presented through a comparison of load–deflection curves obtained from experimental tests, full models and web-post models, according to Fig. 3. According to the results obtained, the difference between FE and experimental shear loads ranges from −8.8% to 9.4%, with an average deviation of −0.14% and a coefficient of variation of 0.14% [1]. These results indicate that the proposed web-post model provides reliable accuracy and is suitable for further parametric studies on shear capacity. Fig. 4 shows an example of FE model under web-post buckling considering full model and web-post model against test performed by Tsavdaridis and D'Mello [8].

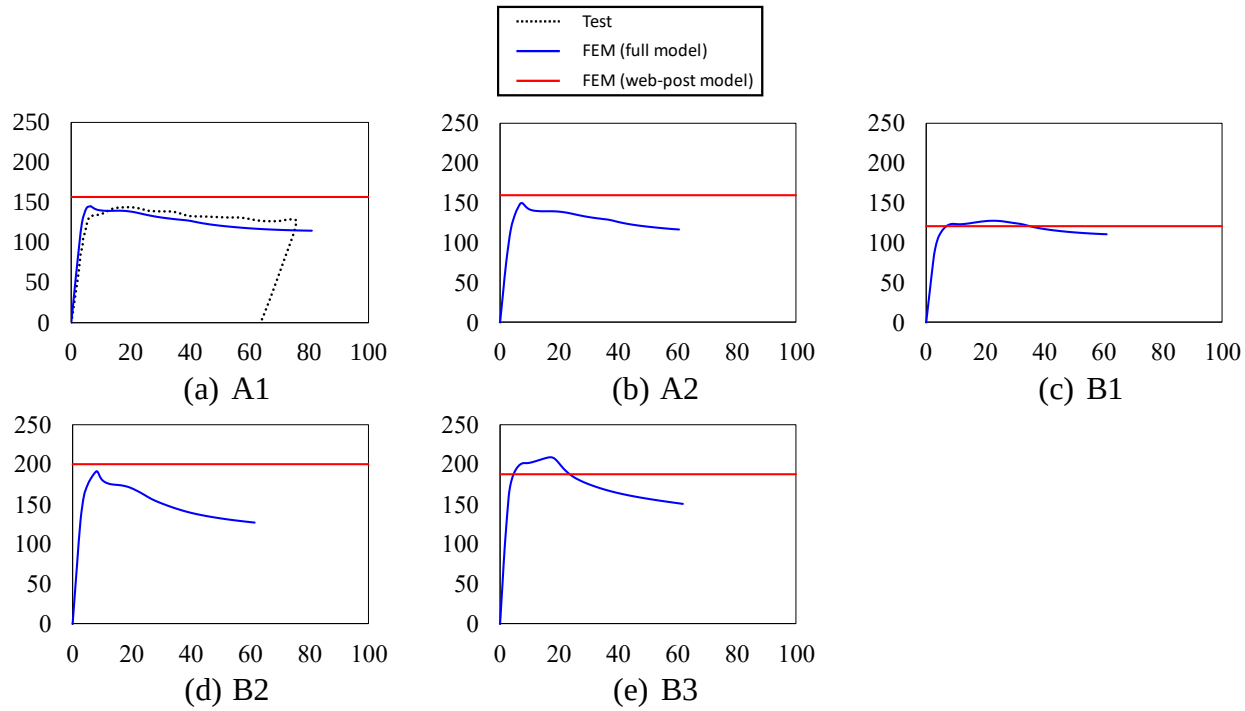


Fig. 3: Global shear (in kN) vs. Mid-span vertical displacement (in mm)

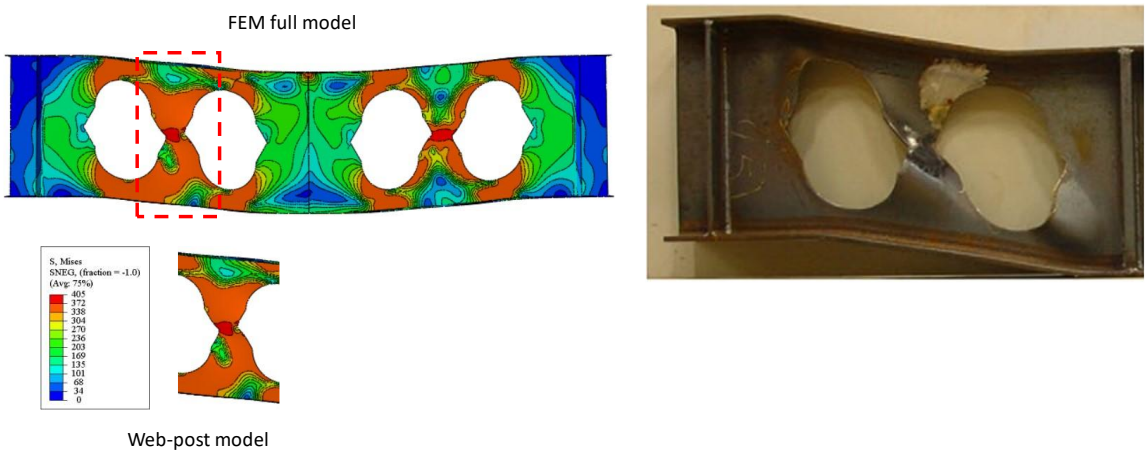


Fig. 4: Web-post buckling via developed FEM

A comprehensive database of 14,353 FE models, considering steel grades S355, S460, S690, and S960 has been developed by the authors, and a more detailed description of the FE model development is available in Ferreira et al. [1,10]. The Python scripts and FE models used in this parametric study are available in the publicly accessible dataset titled "Database of Finite Element Method Predictions for Web-Post Buckling Resistance of Steel Beams with Elliptically-Based Web Openings" [40]. This resource provides all necessary files for reproducing the simulations, including model geometries, boundary conditions, material definitions, and analysis procedures, allowing other researchers to verify results or extend the work for further investigation [43].

While the generated dataset covers a broad and validated range of structural configurations, it is based on idealised FEM simulations. As such, potential biases related to real-world fabrication tolerances or non-modelled imperfections may still affect practical application.

3.2. Data Preprocessing

The data preprocessing stage is fundamental to ensuring the dataset is clean, structured, and compatible with ML algorithms. It begins with loading the raw dataset, inspecting its structure, and verifying the completeness of the records. The next step involves separating the dataset into input features and output targets, where predictors are the independent variables influencing the model and the targets represent the dependent variables to be predicted.

3.3. Statistical Evaluation

The database covers a wide range of web-post geometries and material properties, as summarized in Table 1, ensuring that the ML models are trained on a diverse set of structural configurations. The statistical descriptors confirm that all variables span sufficiently broad intervals, with coefficients of variation between 0.38 and 0.87, indicating a balanced spread suitable for generalisation.

Table 1: Statistical analysis of the database

	Minimum	Maximum	Mean	Standard deviation	Coefficient of variation
***d* (mm)**	177.8	834.9	476.9	196.2	0.41
***b_f* (mm)**	101.2	320.2	183.4	76.6	0.42
***t_f* (mm)**	7.0	37.6	16.9	8.4	0.50
***t_w* (mm)**	4.8	21.1	10.7	4.6	0.43
***h* (mm)**	221.3	1354.6	688.7	290.5	0.42
***h_0* (mm)**	138.7	1202.3	508.1	229.1	0.45
***a_0* (mm)**	34.7	781.5	257.4	137.1	0.53
***s* (mm)**	62.4	1502.8	424.9	229.2	0.54
***f_y* (MPa)**	355	960	616.3	232.5	0.38
WPB (kN)	39.4	4212.8	729.7	636.9	0.87

To complement the tabulated metrics, **Fig 5** presents the distributions of both input features and output targets in a compact form. Input variables (WPB, h, s, a_0, h_0) are displayed as violin plots, which highlight their median values, interquartile ranges, and overall variability. This representation makes clear the skewed distributions of s and h, as well as the wider spread of WPB compared with geometric descriptors.

For the output targets (d, b_f, t_w, t_f, f_y), standardized ridgeline plots are used. Each variable is normalized to z-scores to allow comparability across scales, since thicknesses (t_f, t_w) are one order of magnitude smaller than section depth or flange width, and yield strength (f_y) is expressed in MPa. The ridgeline plots reveal distinct distributional patterns: d and b_f are moderately skewed with long right tails, t_w and t_f cluster tightly around their means with narrow spread, and f_y exhibits a bimodal tendency reflecting the inclusion of both standard- and high-strength steels in the dataset.

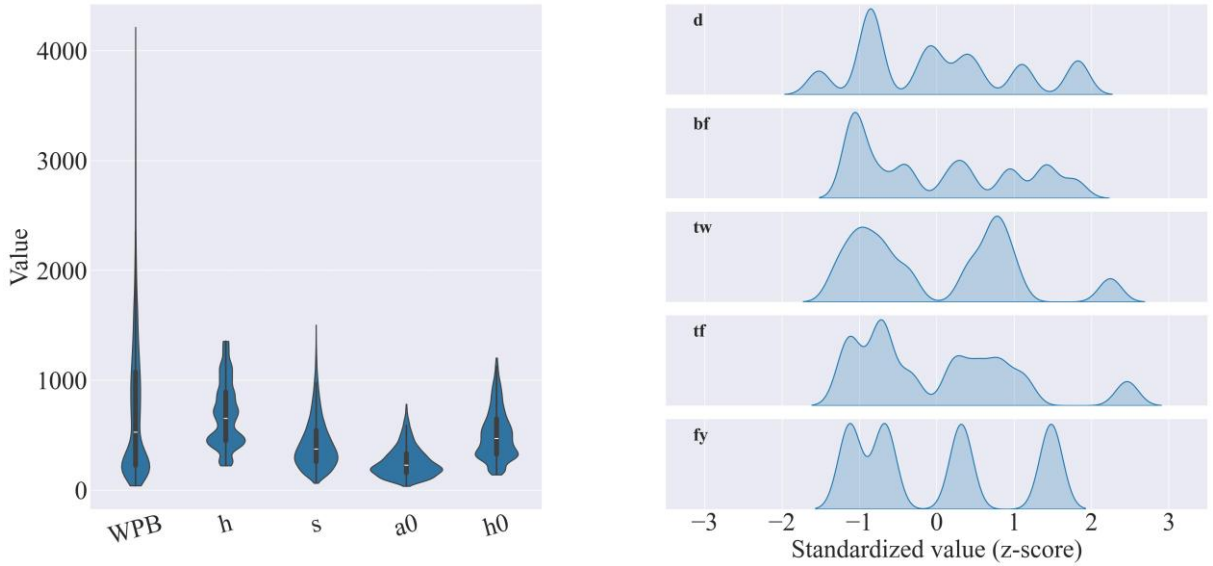


Fig.5: Statistical representation of the database: violin plots for input features (WPB, h, s, a_0, h_0) and ridgeline plots for output targets (d, b_f, t_w, t_f, f_y).

3.4. Correlation Evaluation

A visual representation of the correlation coefficients between the studied parameters, as derived from the dataset, is displayed in Fig. 6. The values range from -1 to 1, where -1 indicates a strong negative correlation, 1 denotes a strong positive correlation, and 0 suggests no correlation between the parameters. Key results derived from the heatmap analysis shown in Fig. 6 are presented below:

1. Overall correlation observations: the feature d (depth) exhibits the strongest correlation with h (height), having a coefficient of 0.97. This suggests a significant interdependence between these geometric parameters. Additionally, b_f (flange width) and t_w (web thickness) are strongly correlated, with a value of 0.92.
2. Influence on Web-Post Buckling (WPB): t_w and t_f show a strong positive correlation with WPB, with coefficients of 0.86 and 0.85, respectively. These parameters directly affect the structural behavior under buckling conditions. Conversely, f_y displays a weaker correlation with WPB (0.29), suggesting a limited direct impact of material strength on post-buckling behavior.
3. Material interdependencies: the parameter f_y exhibits negligible correlations with geometric properties such as d, b_f, t_w, and t_f (all close to 0.00). A similar trend is observed between f_y and derived parameters such as a_0 and h_0, highlighting its independence from the section's geometric configuration.
4. Geometric interdependencies: strong interdependencies are observed among several geometric parameters. For instance, a_0 and s show a very-high positive correlation of 0.97, indicating that these parameters are closely related in their derivation or measurement. Similarly, the

parameters h_0 and h exhibit a strong correlation (0.97), emphasizing their proportional relationship in structural design.

5. Negligible and moderate correlations: certain parameters, such as f_y and h, show negligible correlations with other features. On the other hand, s exhibits moderate positive correlations with b_f and t_w (0.69 and 0.53, respectively), indicating a partial influence of flange width and web thickness on the derived spacing parameter.

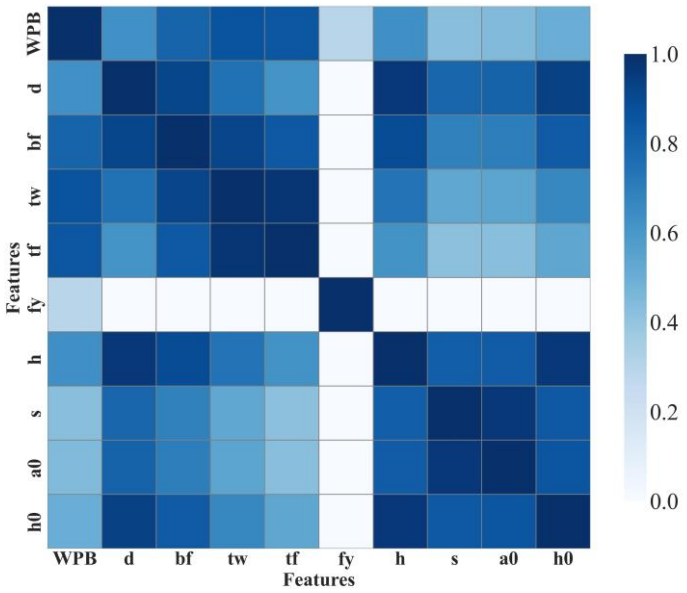
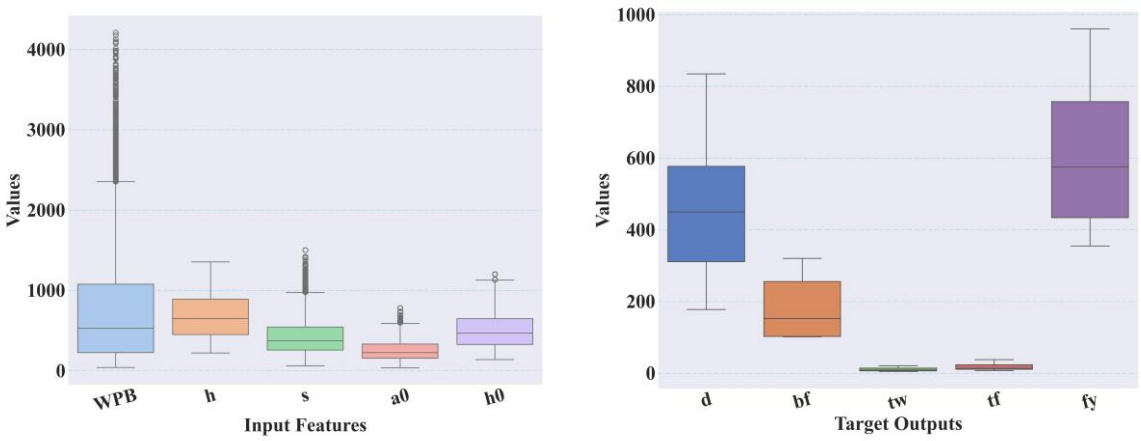


Fig. 6: Correlation heatmap

3.5. Distribution and Variability Analysis of Input and Output Features

Fig. 7 for the input and output features highlight the statistical distribution, variability, and presence of outliers across the dataset. Among the input features, WPB shows the largest range and numerous outliers, reflecting high variability, while h and s show moderate distributions with limited extreme values. Features a_0 and h_0 are more uniform, with a_0 having the smallest range. For the output features, d and f_y exhibit broader ranges, with f_y showing significant variability due to differences in material properties. Conversely, b_f, t_w, and t_f have narrower ranges, with t_w and t_f being the most uniform. Notably, outliers were retained in the analysis as they did not adversely impact the ML models.



(a) (b)

Fig. 7: Visualisation of box plots representing (a) input features and (b) target outputs.

4. Development of ML Models

In this study, five supervised ML algorithms were selected and implemented using the Scikit-learn library [44] to predict the parent section and material properties of perforated steel beams. These models include Histogram-Based Gradient Boosting (HistGB), Extreme Gradient Boosting (XGB), Random Forest (RF), k-Nearest Neighbors (KNN), and Support Vector Regression (SVR). Together, they represent a diverse mix of tree-based, kernel-based, and non-parametric techniques, allowing us to evaluate the problem from different modelling perspectives [45].

The choice of these models was motivated by their track record in structural engineering applications. For example, tree-based ensemble methods like HistGB and XGB are known for their ability to handle nonlinear feature interactions and large datasets efficiently [46–49]. RF is a reliable baseline for many regression tasks and offers useful insights into feature importance [50,51]. KNN provides a simple but effective approach for local pattern recognition, while SVR is often preferred when dealing with small datasets or problems requiring high precision [52–56].

Rather than repeating standard algorithm descriptions, which are available in numerous studies, we refer the reader to [45], which offers a recent and well-rounded review of these models in structural design and material prediction contexts. That paper covers the theoretical background, practical applications, and performance trade-offs of each algorithm. Here, we focus on applying and comparing them in the context of inverse structural design. Their specific roles and comparative results are discussed in the next sections.

4.1. Evaluation Metrics

The performance of the ML models in this study is evaluated using three widely recognised metrics: the Coefficient of Determination (R^2), Root Mean Square Error (RMSE), and Mean Absolute Error

(MAE). R^2 measures how well the model explains the variability in the target variable, with values closer to 1 indicating better predictive accuracy. RMSE quantifies the average magnitude of prediction errors, emphasising larger deviations due to the squaring process, making it suitable for scenarios where significant errors are critical. In contrast, MAE provides the average magnitude of errors without additional weighting for larger deviations, offering a straightforward and balanced measure of prediction accuracy.

4.2. Model training and hyperparameter optimization

The training process of ML models involves selecting optimal hyperparameters and splitting the dataset to ensure the models are both accurate and robust. Hyperparameters are critical settings that govern how an ML model learns and performs. To achieve optimal performance, various search strategies are employed to explore the hyperparameter space systematically. In this study, both randomized search and grid search methods were utilized to identify the best hyperparameters. Initially, random search was used to select hyperparameter values from predefined ranges, testing a variety of combinations in a stochastic manner. This was followed by grid search, which performed an exhaustive evaluation of all possible combinations within the specified ranges. These two methods complemented each other by balancing exploration and precision in identifying effective hyperparameters. To further enhance model reliability and prevent overfitting, a 10-fold cross-validation algorithm was employed [44]. This approach involved splitting the training data into ten equal parts and iteratively using each partition as a validation set while the others served as the training set. This process ensured that the evaluation was not biased by a specific subset of the data and provided a more robust estimate of the model's performance. Table 2 presents a detailed summary of the hyperparameter values evaluated for each ML model, including both the search ranges and the final configurations selected during the optimization process.

Table 2. Hyperparameter Optimisation Summary

Model	Search space	Selected value				
		d	**t_f**	**t_w**	**b_f**	**f_y**
Random Forest	n_estimators: [100, 200, 300]	200	200	300	200	100
	max_depth: [None, 5, 10, 20]	None	None	None	None	None
	min_samples_split: [2, 10, 20]	2	2	2	2	2
	min_samples_leaf: [1, 5, 10]	1	1	1	1	1
	bootstrap: [True, False]	True	True	True	True	True
XGBoost	colsample_bytree: [0.8, 1.0, 1.2]	0.8	0.8	0.8	0.8	0.8
	gamma: [0, 0.01, 0.1]	0	0	0.01	0	0.1
	learning_rate: [0.01, 0.1, 0.2, 0.3]	0.1	0.1	0.1	0.1	0.3
	max_depth: [2, 4, 6]	4	4	4	4	4
	min_child_weight: [1, 4, 7]	1	1	1	1	1
	n_estimators: [50, 100, 200]	100	200	100	50	50
	reg_alpha: [0.01, 0.1, 1.0]	0.01	0.1	0.01	0.1	0.01
	reg_lambda: [0, 0.001, 0.01, 0.1]	0.001	0.001	0.001	0	0.1

	subsample: [0.8, 1.0, 1.2]	0.8	0.8	0.8	0.8	1.0
KNN	Weights: [uniform, distance]	distance	distance	distance	distance	distance
	Metric: [euclidean, Manhattan]	Manhattan	Manhattan	Manhattan	Manhattan	Manhattan
	n_neighbors: [3,5,7,10]	3	5	5	7	5
Histogram-Based	learning_rate: [0.01, 0.1, 0.2, 0.3]	0.1	0.1	0.1	0.1	0.1
Gradient Boosting	max_iter: [100, 200, 300]	200	200	300	100	200
	max_depth: [None, 10, 20, 30]	10	10	20	10	30
	min_samples_leaf: [1, 5, 10, 20]	1	1	1	5	1
	l2_regularisation: [0, 0.01, 0.1, 0.5]	0.1	0.5	0.1	0.01	0.5
Support Vector Regressor	kernel: ['linear', 'poly', 'rbf', 'sigmoid']	rbf	rbf	rbf	rbf	'poly'
	C: [0.01, 0.1, 1.0, 10.0, 100.0, 1000.0]	10	10	10	10	1000
	epsilon: [0.001, 0.01, 0.2, 1.0, 10.0]					
	gamma: ['scale', 'auto', 0.001, 0.01, 0.1, 1.0, 10.0]	0.2 scale	0.2 scale	0.2 scale	0.01 scale	0.01 scale

The prepared and scaled dataset was divided into two subsets: a training set and a testing set. To ensure a balanced and practical approach, 70% of the data (10,047 sample) was allocated for training, while the remaining 30% (4,306 sample) was reserved for testing. The 70/30 train-test split was selected after also testing 75/25 and 80/20 configurations, which showed minimal variation in model performance. The 70/30 split provided reliable and consistent evaluation while preserving a large test set for robust validation. The testing data was kept unseen during the training phase to provide an unbiased evaluation of the model's predictive capabilities. By following this strategy, the models were trained to generalize effectively while maintaining high accuracy when applied to new, unseen data. Fig. 8 illustrates the overall methodology adopted for training the machine learning models.

To address overfitting, a 10-fold cross-validation procedure and hyperparameter tuning were adopted. The consistency of training and testing errors, confirmed through residual analysis, demonstrates that overfitting was effectively avoided.

To improve clarity and reproducibility, the complete model training and evaluation process is summarized in Fig. 8. The workflow begins with the import of the full database containing 14,353 samples, which is randomly divided into 70% training data (10,047 samples) and 30% testing data (4,306 samples). One of the candidate algorithms (HistGB, RF, XGB, KNN, or SVR) is then selected for model development. Hyperparameter optimization is carried out using random search followed by grid search, where model performance is estimated by 10-fold cross-validation applied exclusively to the training set. After the best hyperparameters are identified, the final model is trained on the complete 70% training dataset. The resulting model is subsequently evaluated once on the independent 30% testing dataset to assess predictive accuracy, with no further tuning performed at this stage. This procedure is repeated for all considered algorithms in order to determine the best-performing model for each target variable. Finally, the validated models are employed to generate reliable predictions for unseen data.

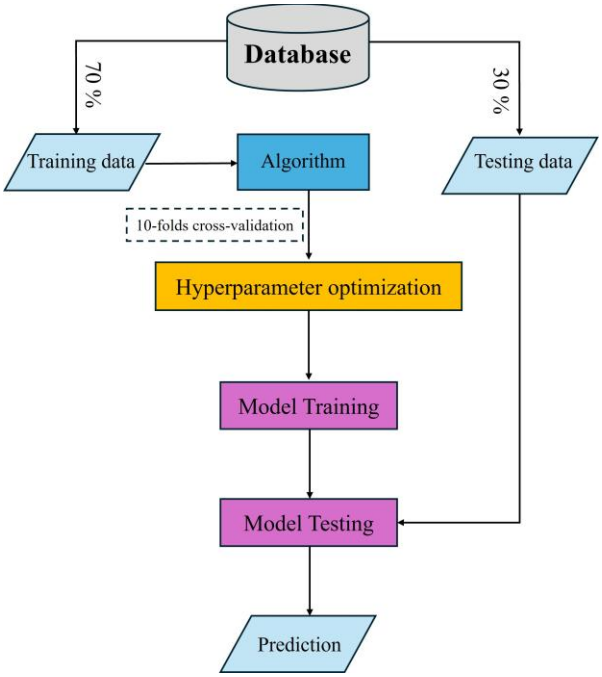


Fig. 8: Flowchart of the ML model development process. Rectangle = Process; Parallelogram = Data Input/Output; Cylinder = Data store.

All ML models were developed and evaluated in Python 3.8.19 on a Windows 10 system. The implementation used the following library versions: scikit-learn 1.3.2, XGBoost 2.0.3, Streamlit 1.34.0, SHAP 0.44.1, NumPy 1.24.3, pandas 2.0.3, joblib 1.4.2, matplotlib 3.7.5, and seaborn 0.13.2. These versions have been fixed across all experiments to ensure reproducibility and consistent behavior across runs.

5. Results and Discussion

5.1 Cross validation scores results

Fig. 9 presents the distribution of R^2 values obtained through 10-fold cross-validation for each model across the five target variables: b_f, d, f_y, t_f, and t_w. Each boxplot represents the interquartile range (IQR), with the median shown as a bold line. Whiskers extend to 1.5×IQR, red circles mark outliers, and blue diamonds indicate mean values.

For b_f and d, HistGB and RF reached the highest accuracy (mean $R^2 \approx 0.99$ and 0.98), with narrow spreads and almost no outliers. KNN and XGB produced intermediate accuracy ($R^2 \approx 0.95$–0.96), while SVR was less stable ($R^2 \approx 0.93$–0.95) and showed wider variability. Prediction of f_y was more challenging. HistGB gave the best performance (mean R2 ≈ 0.93), followed by KNN and RF (≈ 0.91 and 0.90). SVR remained lowest (≈ 0.89), which indicates its limited ability to capture nonlinear relationships in material strength prediction. For t_f, HistGB again dominated (mean $R^2 \approx 0.99$), with RF close behind (≈ 0.97) but showing a few outliers. KNN and XGB achieved moderate accuracy (≈

0.94–0.95), and SVR was again lowest (≈ 0.89). For t_w, HistGB and RF delivered top accuracy (≈ 0.99 and 0.97), KNN and XGB followed (≈ 0.94–0.95), while SVR trailed (≈ 0.90) with a broader distribution.

Overall, ensemble models, and especially HistGB, showed the most reliable performance across all targets. SVR consistently underperformed, particularly for f_y and t_f, where nonlinear effects are more significant.

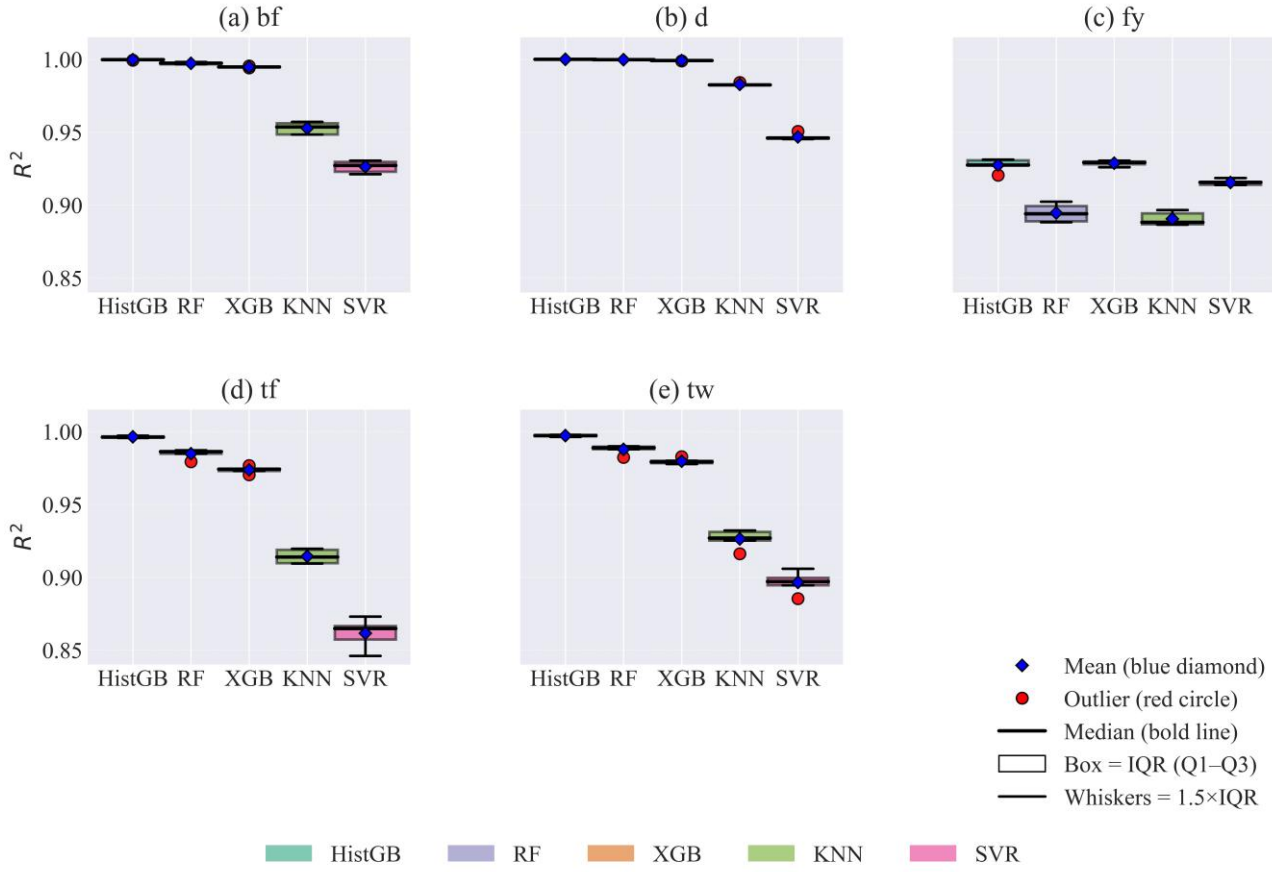


Fig. 9: Distribution of R^2 Values from 10-Fold Cross-Validation for Each Model considering: (a) b_f; (b) d; (c) f_y; (d) t_f; (e) t_w outputs

5.2 Evaluation results of ML models performance

The performance of the five ML models (HistGB, SVR, XGB, KNN, and RF) was assessed using R^2, MAE, and RMSE across training, testing, and combined datasets for all five outputs (d, b_f, t_w, t_f, f_y), as shown in Figs. 10–12.

For d and b_f, HistGB consistently achieved near-perfect R^2 values (~0.999), with the lowest MAE and RMSE across all data splits. RF also performed well (R^2 ≈ 0.998) with moderate errors, while XGB showed slightly higher MAE (~3.5) and RMSE (~6.0). KNN showed acceptable R^2 values

(>0.95) but suffered from larger errors, especially on testing data. SVR recorded the weakest performance, with R^2 falling to ~0.94 and the highest MAE and RMSE values in both cases.

For t_w and t_f, HistGB again led with $R^2 > 0.998$ and the lowest error metrics. RF and XGB followed closely, particularly RF for t_w and XGB for t_f. KNN showed moderate to good accuracy but with greater variability. SVR performed poorly on both outputs, with $R^2 < 0.90$ and RMSE values nearly double those of the leading models.

In the case of f_y, the model rankings shifted: SVR achieved the highest R^2 (~0.96) but still exhibited relatively high error margins (MAE ~25, RMSE ~46). HistGB, XGB, and RF followed with slightly lower R^2 (0.94–0.95) but greater consistency across all datasets. KNN remained the weakest for f_y, with the highest errors and lowest R^2 (~0.91).

While all five ML models contributed to the non-iterative prediction framework, their individual strengths varied depending on the output. HistGB consistently outperformed other models for d, b_f, t_w, and t_f, combining very high accuracy with low error variance. This is explained by its ensemble boosting mechanism, which adaptively partitions structured nonlinear relationships between opening geometry, web-post buckling, and section dimensions. In contrast, f_y showed weaker direct correlations with geometry and resistance features; here SVR, with its kernel-based mapping, was better suited to capture subtle nonlinear patterns, achieving the highest R^2 despite larger error margins. This dual evidence, from cross-validation metrics, residual analysis, and model mechanisms justifies the choice of HistGB for geometric outputs and SVR for yield strength as the most reliable predictors in the framework.

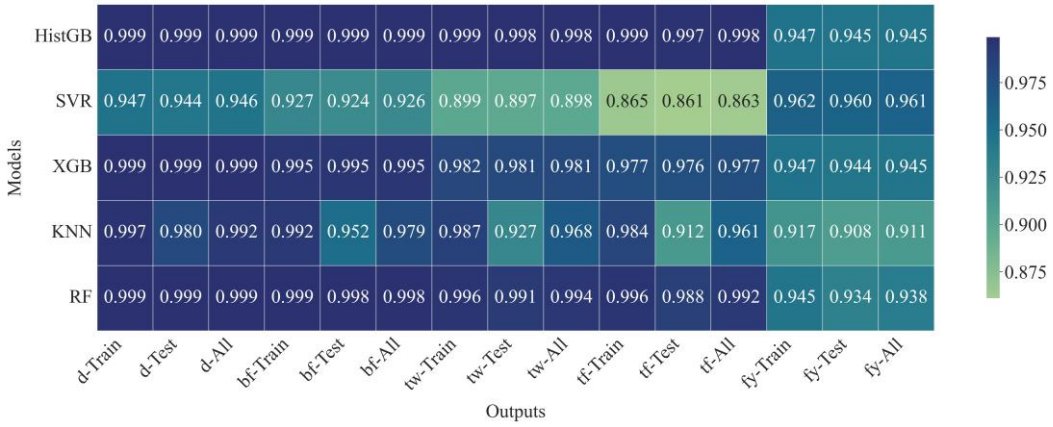


Fig. 10: Heatmap of R^2 values for all models, outputs, and datasets.

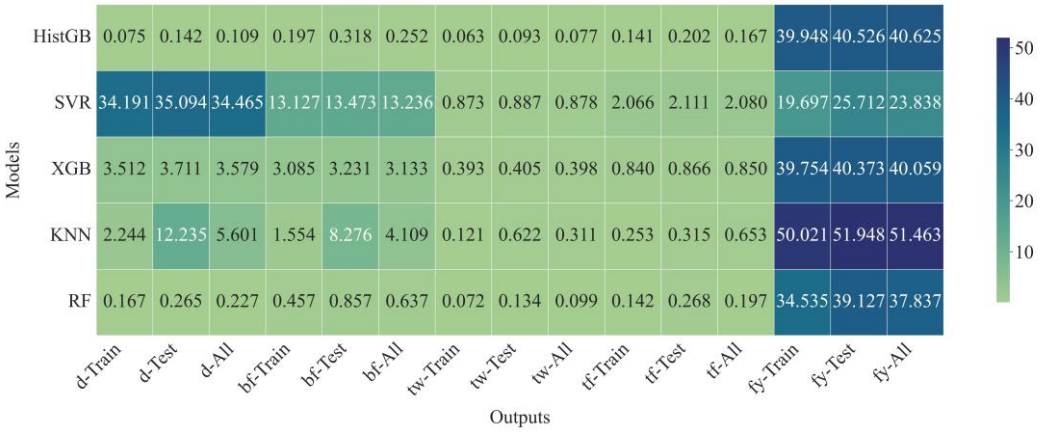
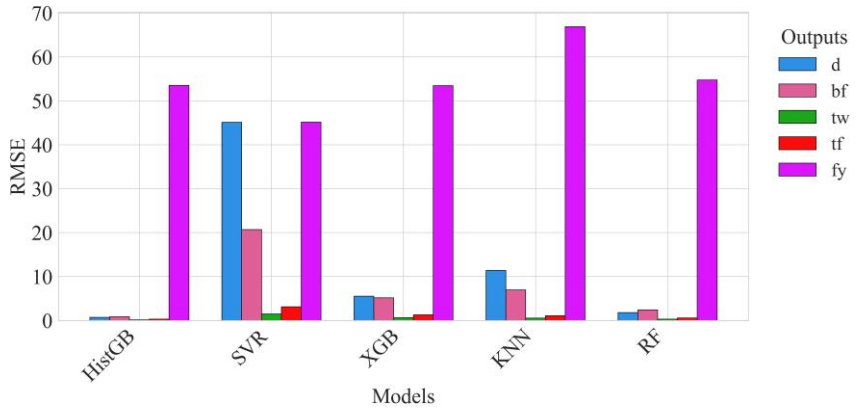
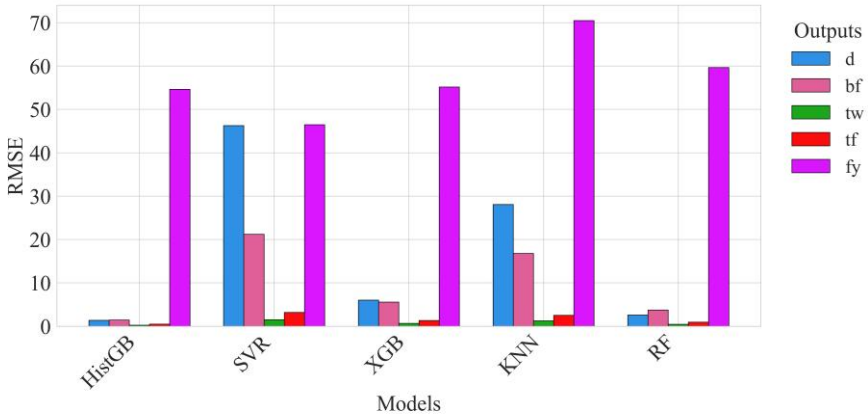


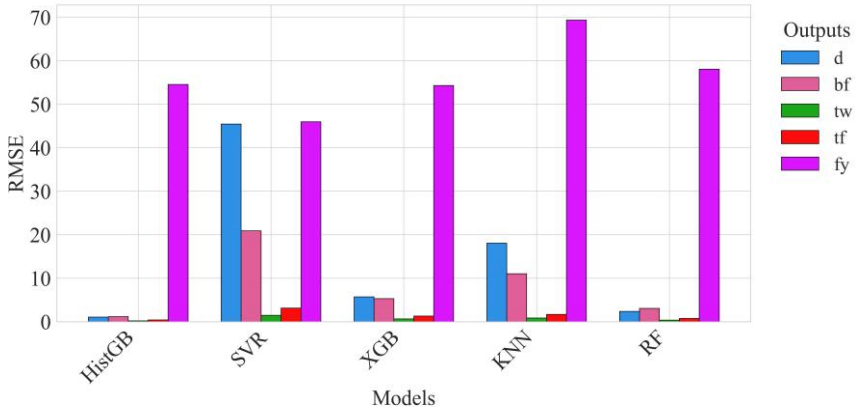
Fig. 11: Heatmap of MAE values for all models, outputs, and datasets.



(a)



(b)



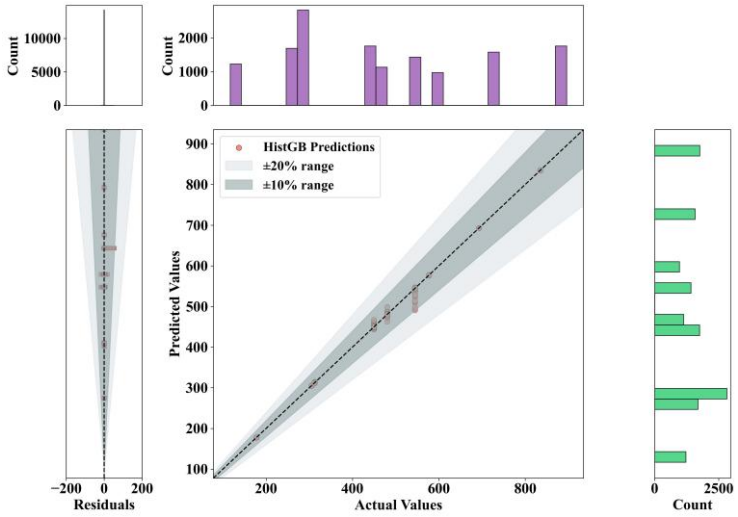
(c)

Fig. 12: Bar chart of RMSE values across all models and outputs for: (a) the training dataset; (b) the testing dataset; and (c) the combined dataset

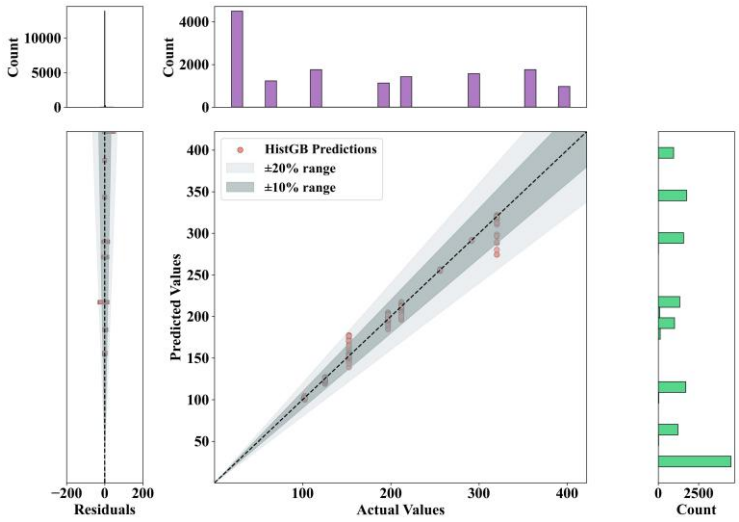
5.3 Evaluation of predicted outcomes against actual results

Fig. 13 compares predicted and actual values for the five output variables (d, b_f, t_w, t_f, f_y) using the best-performing models, HistGB for geometric parameters and SVR for yield strength. Each subfigure shows scatter plots (predicted vs. actual), residual distributions, and ±10% and ±20% error bands for visual accuracy assessment. For d (Fig. 13a), predictions closely follow the 1:1 line, with nearly all samples within ±10%. Residuals are symmetrically distributed around zero, and the predicted and actual histograms overlap almost perfectly, confirming high reliability. Similar accuracy is observed for b_f (Fig. 13b) and t_w (Fig. 13c), where values remain tightly clustered along the ideal line and very few outliers appear. Residuals are evenly dispersed, again confirming the robustness of HistGB. For $\mathbf{t_f}$ (Fig. 13d), the results remain strong. Predictions fall predominantly within the ±10% band, with residuals narrowly centered on zero. The close match of distribution shapes highlights low variance and model fidelity. For f_y (Fig. 13e), the SVR model shows slightly greater dispersion. While most predictions fall within ±10% and ±20%, the scatter is less compact than for geometric outputs. Residuals show a wider spread, and the distributions of predicted and actual values diverge slightly, indicating reasonable but less consistent accuracy compared to HistGB.

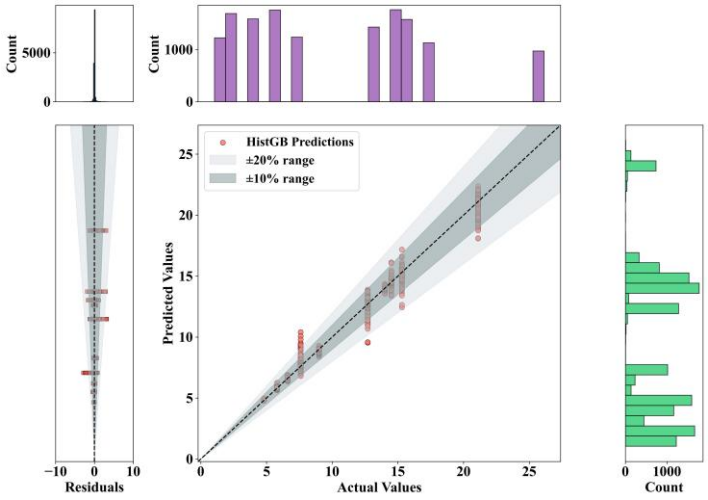
The database encodes parent sections as standard UB catalogue sizes and material as a discrete set of grades, so the inverse model is trained on a quantized label space. In predicted-vs-actual plots (Fig. 13) this appears as vertical stacks at catalogue levels. This is intentional and mirrors practice, where deliverables must map to buildable, code-compliant options. The effect does not reflect model bias: residuals remain centered with narrow spread (Fig. 14), and cross-validated metrics are high. In contexts that permit non-catalogue tailoring, the same workflow can be run with a denser label set or with a continuous prediction followed by nearest-catalogue mapping.


Count
10000
5000
0
Count
2000
1000
0
HistGB Predictions
±20% range
±10% range
Predicted Values
Actual Values
Residuals
−200
0
200
Count
2500

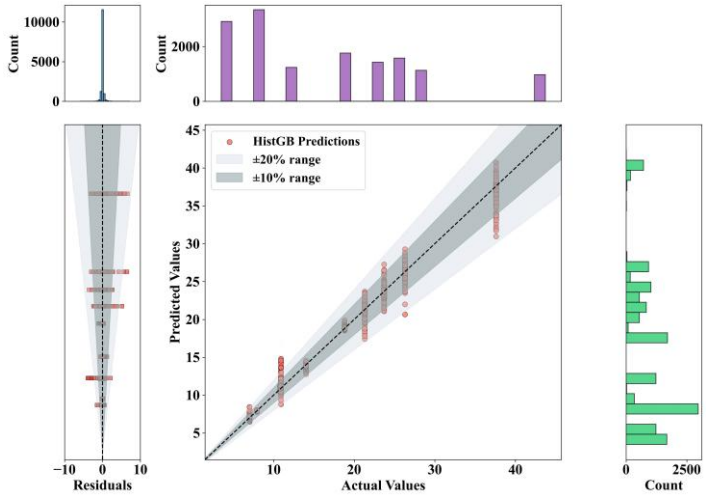
(a)


Count
10000
5000
0
Count
4000
2000
0
HistGB Predictions
±20% range
±10% range
Predicted Values
Actual Values
Residuals
−200
0
200
Count
2500

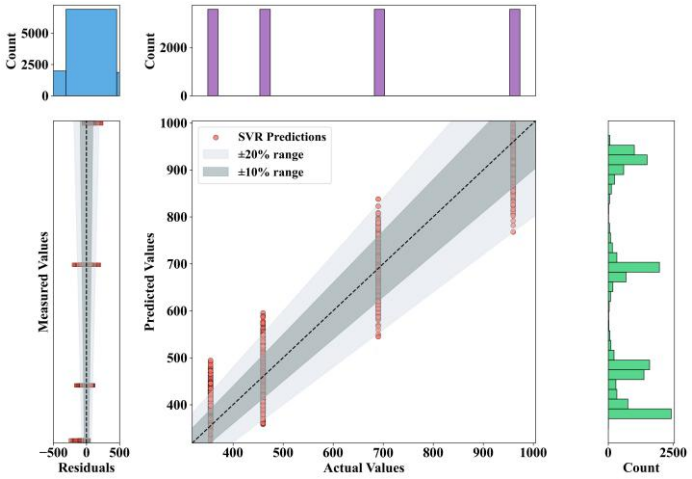
(b)


Count
5000
0
Count
1000
0
HistGB Predictions
±20% range
±10% range
Predicted Values
Actual Values
Residuals
−10
0
10
Count
1000

(c)



(d)



(e)

Fig.13: Combined comparison of actual vs. predicted results for all outputs: (a) d; (b) b_f; (c) t_w; (d) t_f; and (e) f_y.

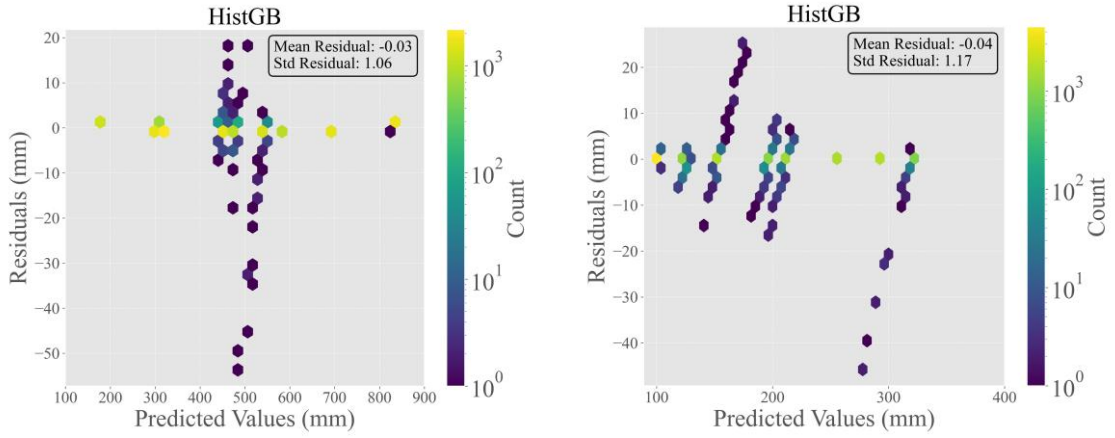
5.4 Analysis of residuals in ML models

Fig.14 presents the residual plots for the best-performing models used to predict each output variable. These plots display the distribution of errors (actual − predicted), along with the mean and standard deviation of residuals, offering a quantitative assessment of accuracy and consistency.

For d and b_f (Figs. 14a–b), the HistGB model achieves tightly clustered residuals around zero, with mean errors of −0.03 mm and −0.04 mm, and standard deviations of 1.06 mm and 1.17 mm, respectively. Both outputs show minimal bias and consistent accuracy across the full prediction range. t_w (Fig. 14c) exhibits the smallest spread, with a mean residual of −0.01 mm and a standard deviation of just 0.18 mm, confirming the exceptional precision of HistGB for this parameter. In t_f (Fig. 14d), the residuals remain symmetrically distributed with a low mean of −0.01 mm and a standard deviation of 0.38 mm, again indicating stable and unbiased predictions. For f_y (Fig. 14e), using the SVR model,

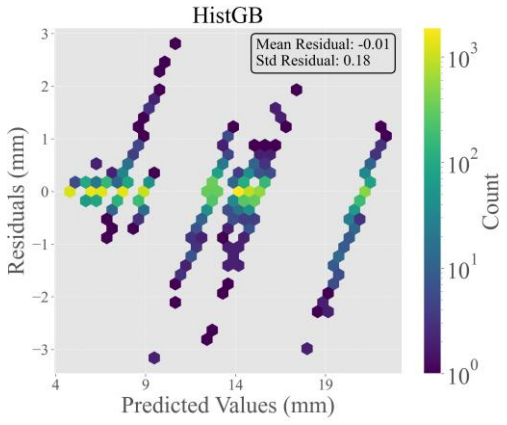
the residuals are more dispersed, particularly at higher predicted values. The mean error is −0.79 MPa and the standard deviation increases to 28.89 MPa, suggesting that while the model performs reasonably, it is less stable than the HistGB model for geometric outputs.

In summary, the residual analysis confirms the consistency and low bias of the HistGB model across all geometric outputs, while highlighting the relative limitations of SVR for predicting yield strength.

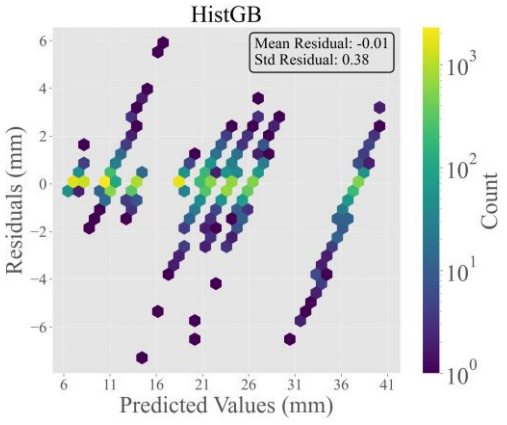


(a)

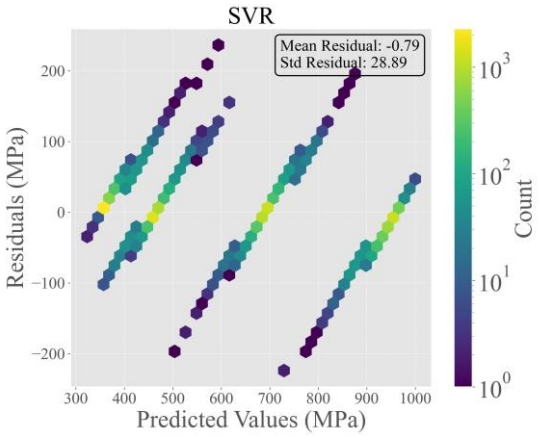
(b)



(c)



(d)



(e)

Fig. 14: Residual analysis plots for the best-performing ML models including the mean residuals and standard deviations, across all outputs (a) d; (b) b_f; (c) t_w; (d) t_f; and (e) f_y.

6. Explainable Machine Learning

Explainable machine learning (XML) enhances the transparency of predictive models by revealing how input features influence outputs. Unlike traditional black-box models, explainable techniques allow users to understand the reasoning behind predictions, detect potential biases, and assess model logic—an essential requirement in structural engineering where safety and reliability are paramount [59–62]. Two related concepts support this goal: explainability refers to methods that uncover the internal structure of a model, while interpretability relates to how easily a user can understand a specific prediction. Both are critical to ensure that advanced ML models remain accessible, trustworthy, and aligned with engineering judgment [63–67].

Explainable artificial intelligence (XAI) focuses on making complex model behavior understandable, consistent, and useful for real-world decision-making. One central objective is building user trust by ensuring that the model behaves in a stable and predictable manner [72–74]. In addition, XAI helps clarify the underlying data relationships that drive predictions, offering insights that can inform design or policy, even if full causal inference is beyond the model's scope [75]. The ability to communicate these relationships in an interpretable way enhances the practical value of ML models by allowing users to apply the results with confidence [60,76]. Moreover, transparency in model behavior supports generalization across tasks, as understanding why a model works in one scenario improves its transferability to related problems [77,78]. Finally, XAI contributes to reliability by making uncertainty visible. Communicating the stability of predictions and confidence in outputs enables engineers to judge whether results are robust enough to be trusted in critical design scenarios [79].

6.1. SHapley Additive exPlanations

Interpretability methods in ML are commonly categorized into two types: model-specific and model-agnostic approaches [54–58]. While model-specific techniques are designed to the internal structure of particular algorithms, model-agnostic methods provide general frameworks applicable across a wide range of models. Among these, SHapley Additive exPlanations (SHAP) has emerged as a widely adopted model-agnostic tool, rooted in cooperative game theory [52].

SHAP uses the concept of Shapley values to quantify the contribution of each input feature to a model's output. In this framework, features are treated as players in a game, and the Shapley value represents the average marginal contribution of a feature across all possible subsets of input variables. This method enables both global and local interpretability: global interpretations summarize feature

importance across the dataset, while local explanations reveal how each feature affects individual predictions. Through these contributions, SHAP has become an essential tool for advancing transparency and interpretability in machine learning. These variables signify the presence or absence of each covariate within the model. An approximation of each prediction, denoted as $f(z)$ is achieved through $g(z')$, where *g* represents a linear function characterized by binary variables (Eq. (1)) [52]:

$$g(z')=\phi_0+\sum_{i=1}^{M}\phi_i z_i' \tag{1}$$

Where, $z'\in\{0,1\}^M$, $\phi_i\in R$.

Here, ϕ_0 shows the base value or expected model output(i.e., the prediction with all features missing), and *M* is the total number of input features in the model.

As a result, the Shapley value of the feature *i* is computed accordingly (Eq. (2)):

$$\phi_i=\sum_{S\subseteq F\setminus\{i\}}\frac{|S|!(|N|-|S|-1)!}{|N|!}[f_{S\cup\{i\}}(x_{S\cup\{i\}})-f_S(x_S)] \tag{2}$$

Where, *S* represents the subset of variables in the model, *N* is the number of input features, x_s represents the value of the features in the input set *S*, $\frac{|S|!(|N|-|S|-1)!}{|N|!}$ is the weight of the subset *S*, which is related to the order.

$f_S(x_S)$ is the prediction of the subset *S*, marginalized on features not included in the set *S* (Eq. (3)):

$$f_S(x_S)=\int\hat{f}(x_1,x_2,...,x_M)dP_{x\notin S}-E_x(\hat{f}(X)) \tag{3}$$

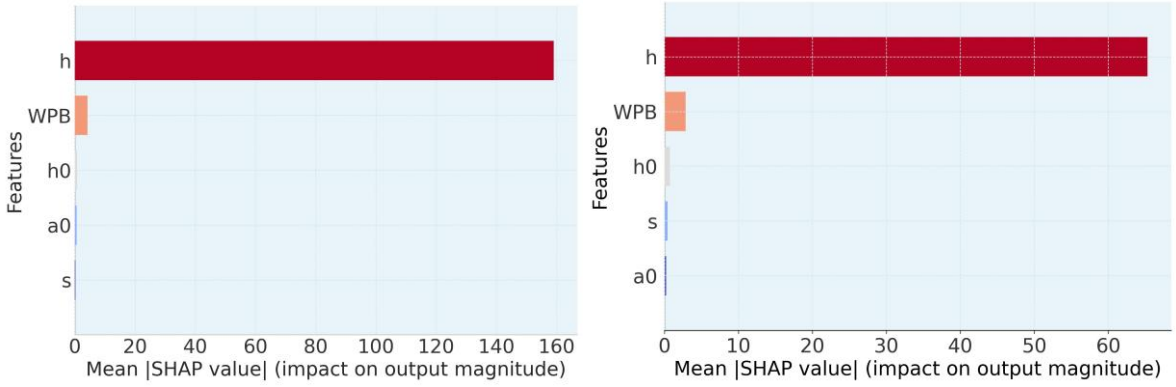
Here, $\hat{f}(x_1,x_2,...,x_M)$ denotes the original machine learning model's prediction using the full input feature set, and *M* is the total number of input features. $P_{x\notin S}$ is their marginal probability distribution. The expectation $E_x(\hat{f}(X)$ corresponds to the model's output averaged over the unknown features.

SHAP's surrogate model provides local and global insights into interpretability. During the prediction process, the Shapley values are computed for each input feature, which represent the importance of each feature in determining the outcome. This process clarifies which input features have consequential or non-contributory effects on the process.

This study initially evaluated five ML models: HistGB, RF, KNN, XGB, and SVR. The detailed evaluation results for these models are fully presented in Section 5. Based on the performance outcomes, the top-performing models were selected for SHAP analysis. Specifically, the HistGB model was utilized for predicting d, b_f, t_f, and t_w, while SVR was chosen for forecasting f_y.

6.2 Analysis of Feature Importance

Fig. 15 presents the feature importance analysis for the five output responses (d, b_f, t_w, t_f, and f_y) based on SHAP values, which evaluate the contribution of each input variable to the model's predictions. The mean absolute SHAP values indicate the relative significance of each feature, with higher values denoting greater influence on the output magnitude. As shown in Fig. 15(a), the feature h overwhelmingly dominates the prediction of d, with a significantly higher mean SHAP value compared to other features. This suggests that h is the most critical variable for predicting d. Other features, such as WPB, h_0, a_0, and s, have minimal contributions. For b_f, Fig. 15(b) also identifies h as the most influential variable, although its dominance is slightly reduced compared to its influence on d. The feature WPB ranks second in importance, contributing a notable but smaller share to the predictions. Similar to d, the remaining features (h_0, a_0, and s) exhibit marginal importance, suggesting that the prediction of b_f is also highly dependent on h. Fig. 15(c) reveals a different pattern for t_f, where WPB emerges as the most significant feature, closely followed by h. The interplay between these two features highlights their joint importance in determining t_f. In contrast, the features h_0, a_0, and s contribute only minor significance. For the output t_w, Fig. 15(d) for t_w shows a similar hierarchy to t_f, with WPB and h again taking the top two positions. WPB holds a slight edge over h, indicating its dominant role. The lesser contributions of h_0, a_0, and s are consistent with their lower SHAP values. Finally, Fig. 15(e) highlights the shared importance of h and WPB in predicting f_y, with both features exhibiting high SHAP values and comparable significance. The feature h_0 also contributes meaningfully to f_y predictions, unlike its role in other outputs, where its impact was negligible. The features a_0 and s show some influence but remain less significant compared to the top three features.



(a) (b)

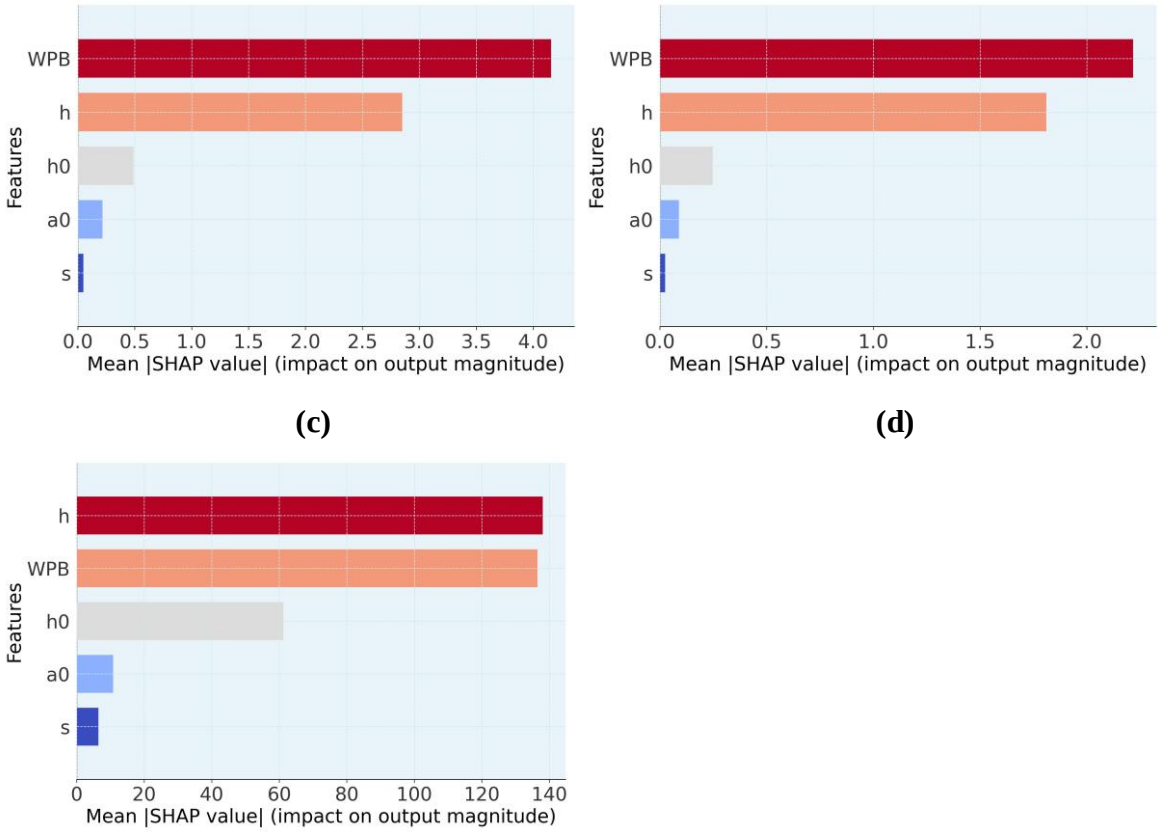
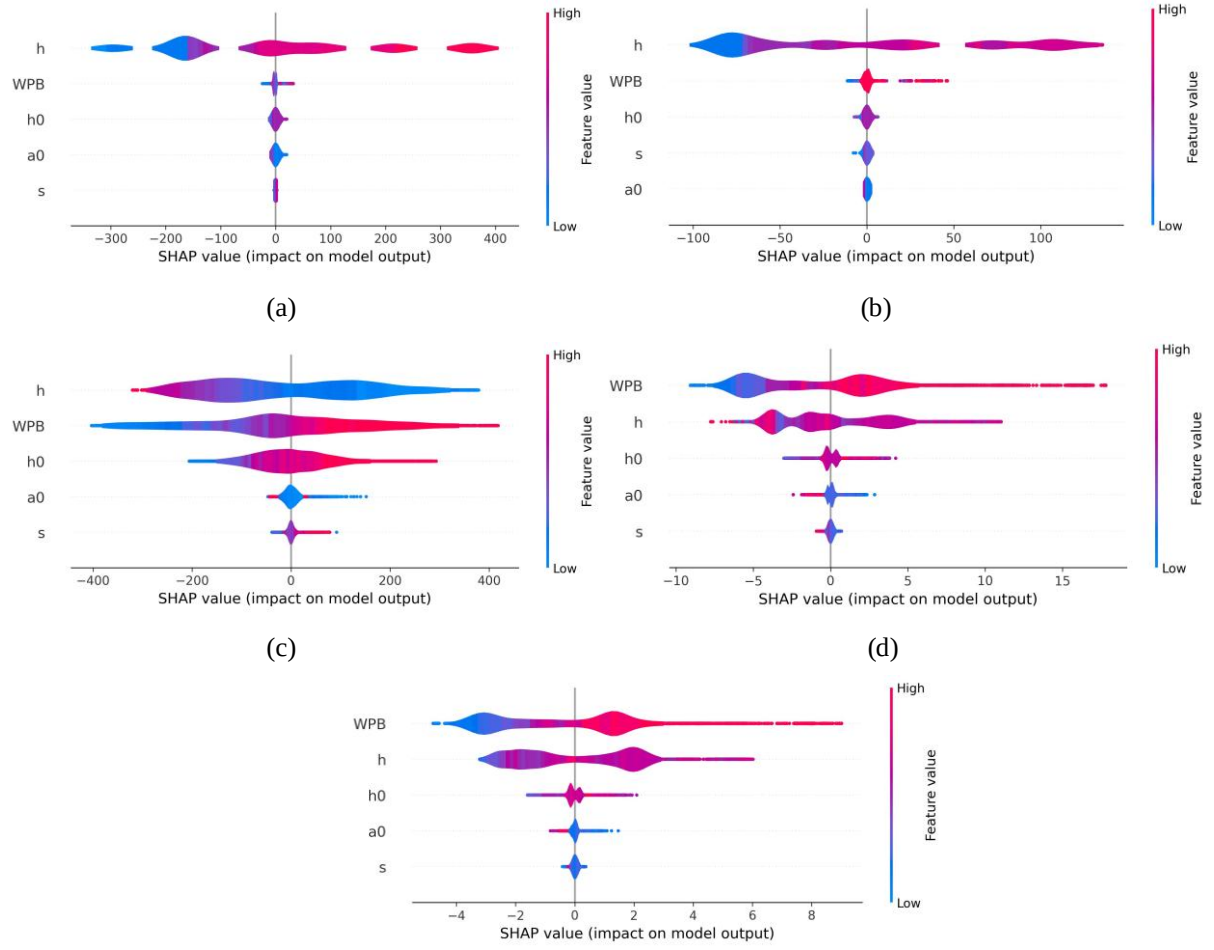


Fig. 15: Feature importance analysis using SHAP Values for predicting outputs: (a): d; (b) b_f; (c): t_w; (d): t_f; and (e): f_y.

6.3. Global Explanation

The SHAP violin summary plots, illustrated in Fig. 16, provide a nuanced understanding of the interplay between input features and their corresponding impact on the predictive model's outputs. These plots reveal not only the magnitude of feature importance but also the directional and distributional trends of their influence, offering critical insights into model behavior. For the prediction of d (Fig. 16(a)), the violin plot for h demonstrates a concentrated density of SHAP values on the positive side, indicating that higher h values reliably increase d. Interestingly, the spread of SHAP values is narrow, suggesting that h has a consistent and predictable effect across the dataset. In contrast, features like WPB and h_0 exhibit a more dispersed SHAP value distribution, implying that their influence varies significantly depending on the specific data instance. This variation underscores the conditional dependency of these features on the context provided by other variables. Fig. 16(b) for b_f highlights h as a pivotal feature, with a symmetric and wide distribution of SHAP values, reflecting its strong influence. Notably, the range of SHAP values for WPB is smaller and more tightly clustered, pointing to a localized effect that impacts specific scenarios rather than providing a broad, uniform influence. This suggests that while h universally drives predictions, WPB contributes in a

more targeted manner depending on the interaction of other inputs. For f_y, Fig. 16(c) shows a striking trend where h exhibits a long tail on the positive side of the distribution, reflecting that extreme values of h significantly boost the predictions of f_y. On the other hand, WPB has a more balanced distribution of SHAP values, implying that while it affects the output, the magnitude of its impact is not as sensitive to extreme values. The violin for h_0 indicates a moderate yet consistent positive effect, suggesting a stable role across the dataset. Fig. 16(d) for t_f reveal interesting contrasts between WPB and h. While both features have positive SHAP values, WPB demonstrates a bimodal distribution, indicating that its impact varies under different scenarios, possibly linked to specific thresholds of other features. In comparison, h exhibits a more uniform trend, suggesting a direct and stable influence. Features such as h_0 and a_0 have narrow distributions, highlighting their relatively weaker and more consistent contributions. Fig. 16(e) for t_w showcases a distinct pattern for WPB, where the density is skewed positively, suggesting that higher values of WPB almost always contribute to increased predictions of t_w. This contrasts with h, which exhibits a more evenly distributed violin, reflecting its balanced role across the dataset. The other features (h_0, a_0, and s) present symmetric, centered distributions with minimal spread, reaffirming their limited and steady influence.



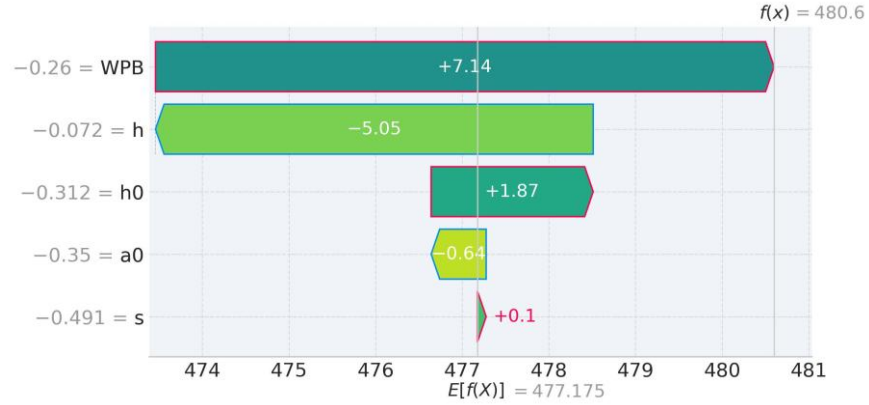
(e)

Fig. 16: SHAP Summary Plots for Global Feature Influence on Outputs: (a) *d*; (b) b_f; (c) t_w; (d) t_f; and (e) f_y.

6.4. Local Explanation

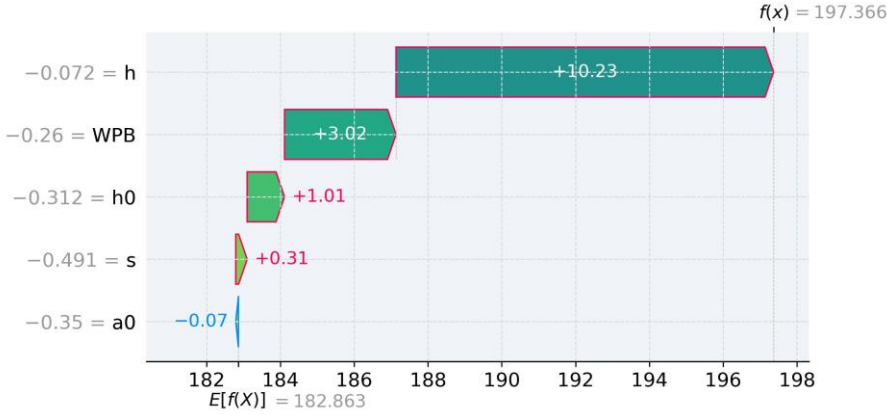
The SHAP waterfall plots provide an intuitive visualization of how the input features contribute to the specific predictions for the given specimen (9234). This method breaks down the prediction into the additive contributions of each feature, starting from the model's base value (expected prediction) and summing the influences to reach the final predicted value.

The predicted value of d for specimen 9234 is 480.6 mm, which is exactly equal to the actual value. As seen in Fig. 17(a), the base value of the model is 477.175 mm, which aligns closely with the general expected depth. The largest positive contribution comes from the WPB, increasing the prediction by +7.14 mm, while the h reduces the depth prediction by -5.05 mm. The other features, such as h_0, a_0, and s, contribute marginally to the final output, indicating their lesser influence on this prediction. As seen in Fig. 17(b), the predicted b_f is 197.37 mm, is slightly overestimated compared to the actual value of 196.7 mm. The model's baseline prediction starts at 182.863 mm and is increased substantially by the WPB feature (+10.23 mm) and to a lesser extent by the section height (+3.02 mm). Negative contributions are observed from the features h_0, s, and a_0, which collectively reduce the prediction by around -0.9 mm. This indicates that the WPB feature is highly influential in determining the flange width. The predicted yield strength (f_y) is 682.55 MPa, which is close to the actual value of 690 MPa. Fig. 17(c) reveals that the WPB parameter dominates the prediction with a significant positive contribution of +186.53 MPa, while h reduces the prediction by -97.56 MPa. Lesser influences are observed for h_0, a_0, and s, which collectively have a minimal effect on the prediction. This suggests that WPB is the primary factor driving the yield strength prediction in this instance. As seen in Fig. 17(d), the predicted flange thickness (t_f) is 26.357 mm, which is slightly higher than the actual value of 26.3 mm. The base value starts at 17.213 mm, and the WPB feature increases the prediction by +4.74 mm, followed by h with an additional contribution of +4.58 mm. Negative contributions are observed for h_0 (−0.18mm) and a_0 (−0.03mm), which indicates that these features have minimal but slightly reducing effects on the prediction. The overall accuracy suggests that WPB and h are key predictors of flange thickness. As seen in Fig. 17(e), the predicted web thickness (t_w) is 15.329 mm, which closely matches the actual value of 15.3 mm. The base value of the model is 10.871 mm, with WPB contributing significantly by adding +2.29 mm. Similarly, h has a substantial positive effect (+2.27mm), while h_0 reduces the prediction by -0.15 mm, and a_0 and s have negligible contributions. This confirms that WPB and h are the dominant features for predicting the web thickness.



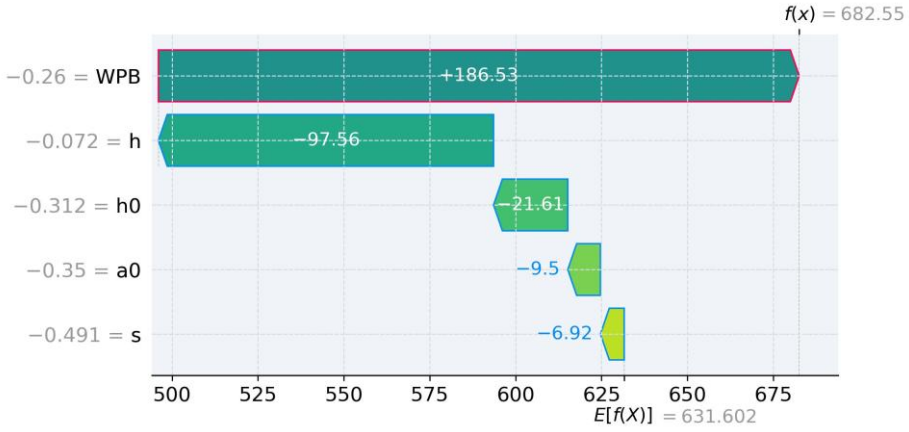
612

613 **(a)**



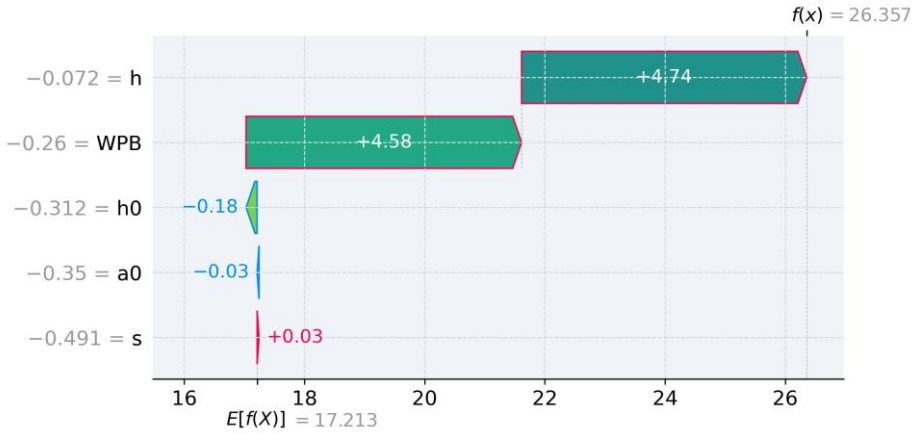
614

615 **(b)**

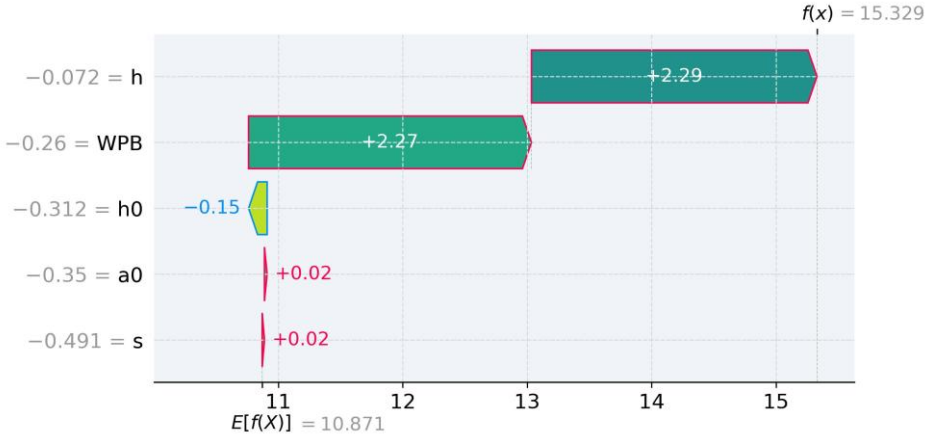


616

617 **(c)**



(d)



(e)

Fig. 17: SHAP Waterfall plots for local explainability of predicted outputs: (a) *d*; (b) b_f; (c) f_y; (d) t_f; and (e) t_w) for Specimen 9234

7. Comparison with Analytical Calculations

This section aims to assess the performance of the proposed inverse machine learning (ML) model through a comprehensive comparison with analytical design model proposed by Ferreira et al. [1,14]. The developed Histogram-based Gradient Boosting (HistGB) is employed due to its outstanding performance, as discussed previously. For this purpose, an extensive dataset was generated with a wide range of input and output parameters, as presented in Table 3. These parameters were employed to derive the analytical predictions of the web-post buckling resistance (WPB), which were subsequently compared then with the WPB values used as input in the inverse ML model.

Table 3: Range of inputs and outputs parameters

	Input	Outputs								
	WPB (kN)	**h (mm)**	**s (mm)**	**a_o (mm)**	**h_o (mm)**	**d (mm)**	**b_f (mm)**	**t_w (mm)**	**t_f (mm)**	**f_y (MPa)**
Min	39.4	221	62	35	139	178	100	4.8	6.5	323
Max	4212.8	1355	1503	781	1202	835	322	22.4	40.7	1000

It is important to highlight that most codified provisions do not include specific design guidelines for web-post buckling resistance with elliptically-based web openings. To address this gap, the recently developed analytical design model proposed by Ferreira et al. [1,14] has been adopted. The key procedures of this model are summarized as follows:

$$l_{eff} = k\sqrt{\left(\frac{h_o - 2R}{2}\right)^2 + \left(\frac{s}{2} - R\right)^2} \tag{4}$$

$$k = 0.516 - 0.288\left(\frac{H}{h_o}\right) + 0.062\left(\frac{s}{s - a_o}\right) + 2.384\left(\frac{s}{a_o}\right) - 2.906\left(\frac{a_o}{h_o}\right) \tag{5}$$

$$\lambda_w = \frac{l_{eff}\sqrt{12}}{t_w} \tag{6}$$

$$f_{cr,w} = \frac{\pi^2 E}{{\lambda_w}^2} \tag{7}$$

$$\lambda_0 = \sqrt{\frac{f_y}{f_{cr,w}}} \tag{8}$$

$$\phi = 0.5\left[1 + 0.49(\lambda_0 - 0.2) + {\lambda_0}^2\right] \tag{9}$$

$$\chi = \frac{1}{\phi + \sqrt{\phi^2 - {\lambda_0}^2}} \leq 1.0 \tag{10}$$

$$\sigma_{Rk} = K\chi f_y \tag{11}$$

$$K = -1.45 + 1.61\left(\frac{H}{h_o}\right) + 0.33\left(\frac{s}{s - a_o}\right) - 0.90\left(\frac{s}{h_o}\right) + 0.21\left(\frac{a_o}{h_o}\right) - 0.004\left(\frac{h_o}{t_w}\right) + 0.49\lambda_0 \quad \text{For } f_y \geq 460 \text{ MPa}$$

$$K = -1.318 + 1.79\left(\frac{H}{h_o}\right) + 0.413\left(\frac{s}{s - a_o}\right) - 1.926\left(\frac{s}{h_o}\right) + 0.937\left(\frac{a_o}{h_o}\right) - 0.02\left(\frac{h_o}{t_w}\right) + 1.412\lambda_0 \quad \text{For } f_y < 460 \text{ MPa} \tag{12}$$

$$V_{EC3} = \sigma_{Rk} t_w (s - a_o) \tag{13}$$

where l_{eff} is the web-post effective length, h_o is the opening height, R is the opening radius, s is the web-post width, H is the distance between flanges centroids, a_o is the opening width, t_w is the web thickness, λ_w is the web-post slenderness factor, $f_{cr,w}$ is the critical stress in the web-post, f_y is the yield strength, λ_0 is a reduced slenderness factor, χ is a reduction factor and V_{EC3} is the global shear – web-post buckling resistance.

Fig. 18 illustrates a comparison between the web-post buckling (WPB) resistance values used in the IML model and those predicted using the analytical model. The results demonstrate excellent agreement with the analytical predictions with a mean ratio of 0.96 and a regression coefficient (R^2) of 0.9805. The Standard Deviation (SD) and Coefficient of Variation (CoV) are both 0.09, reflecting a

consistent performance with low variability. Furthermore, the Mean Absolute Error (MAE) and the Root Mean Square Error (RMSE) are 30 kN and 98.6 kN, respectively. These statistical metrics confirm that the IML is a reliable and efficient tool for designing the WPB resistance of steel beam with elliptically-based web openings.

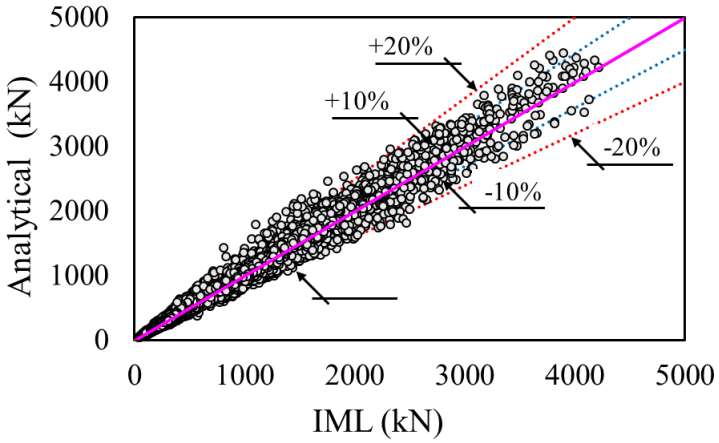


Fig. 18: Performance of the inverse ML model in comparison with the analytical model proposed by Ferreira et al. [1,14].

This level of agreement supports the suitability of the proposed framework not only for current structural design tasks but also as a foundation for broader engineering applications. Beyond steel beam design, the inverse learning methodology may be adapted to more complex structural systems that involve nonlinear geometries or heterogeneous material properties. For example, recent studies have demonstrated data-driven approaches for vibration performance analysis in composite doubly-curved shells [80] and fracture behavior modelling in random porous materials using phase-field techniques [81]. These directions suggest that the proposed inverse ML strategy could be extended to new classes of problems where traditional modelling approaches are limited, thereby enhancing its value as a general-purpose design and analysis tool.

8. Web App

A user-friendly web application was developed using the Streamlit framework to predict parent section properties and material characteristics of steel beams with periodic web openings. The application integrates the trained ML models developed in this study, specifically Histogram-based Gradient Boosting (HistGB) for predicting geometric properties, such as depth (d), flange width (b_f), web thickness (t_w), flange thickness (t_f), and Support Vector Regression (SVR) for predicting the yield strength (f_y).

The backend of the application is designed to ensure accurate predictions while maintaining computational efficiency. The workflow begins with user inputs for the five primary features: web-post buckling force (*WPB*), section height (h), horizontal spacing (s), web opening height (a_0), and initial web-post height (h_0). These input features are entered via interactive sliders and number input fields in the application interface. A key enhancement to the interface includes validation mechanisms to ensure that all input values fall within the valid range used during model training. If a user attempts to input a value outside the allowed range, an error message is displayed, prompting the user to adjust the input accordingly. To prepare the inputs for the ML models, the data is scaled using a MinMaxScaler, which normalizes the input feature values to the range of -1 to 1. This scaling process ensures consistency with the range used during model training, preventing inaccuracies due to out-of-range inputs. The trained models, saved in .joblib format, are dynamically loaded during runtime. A dedicated function checks for the presence of these models and handles their retrieval, ensuring seamless execution. The prediction process involves passing the scaled input features to the corresponding ML models: For geometric properties (d, b_f, t_f, and t_w), predictions are generated using the HistGB model, which was selected due to its superior performance in this study. For yield strength (f_y), predictions are generated using the SVR model, optimized for accurate regression outcomes. The predicted outputs are further refined through a nearest matching algorithm. The predicted outputs are compared against a reference database of standard steel sections, identifying the closest match in terms of geometric properties. The corresponding Universal Beam (UB) designation, along with its standardized properties (depth, flange width, web thickness, and flange thickness), is displayed. Similarly, the predicted yield strength (f_y) is compared against a predefined list of material grades to identify the nearest standard value, enhancing the practical relevance of the predictions. The results are displayed in an organized manner, presenting both the predicted values and the closest standardized section properties. Additionally, a visual representation of structural features is provided using an illustrative image, which enhances user understanding of the beam's characteristics. A screenshot of the web application interface is provided as Fig. 19. The application is available online [82]. The deployed version of the application opens and runs on any web browser across devices, including desktops and mobile platforms. This new application provides a reliable and efficient decision-support tool for structural engineers and researchers. By automating the prediction of parent section and material properties, the tool eliminates the need for manual calculations and iterative testing, enabling faster and more informed decision-making in the design of steel beams with periodic web openings. The application is robust, lightweight, and capable of running online with minimal computational requirements. To ensure trustworthiness, the web application relies on validated machine learning

models, restricts inputs to the trained data domain, and incorporates explainability methods to reveal how predictions are made. In addition, the tool was tested on a wide set of randomly sampled design cases, and its predictions were compared to those from the standalone trained models; the results matched exactly, confirming correct integration of the ML logic into the user-facing interface.

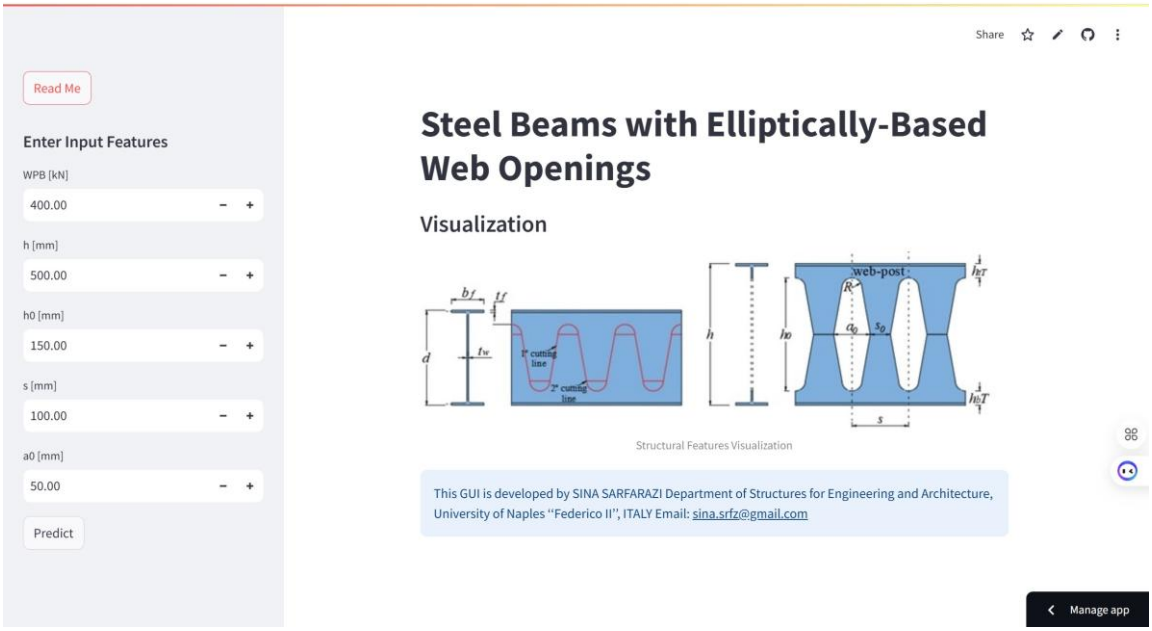


Fig. 19: User interface of the web application

9. Concluding Remarks

This study presents an innovative framework for inverse design in structural engineering, focusing on predicting the parent cross-sectional and material properties of steel beams with elliptically-based web openings. By reframing structural design as an inverse problem, the research eliminates the need for computationally expensive optimization methods and iterative refinement. The proposed methodology utilizes advanced machine learning models (HistGB, RF, XGB, KNN, and SVR) to directly predict key properties such as section depth (d), flange width (b_f), web thickness (t_w), flange thickness (t_f), and yield strength (f_y) based on opening geometric and resistance parameters.

- The results demonstrated very good predictive performance, with R^2 values exceeding 0.99 for most outputs. The HistGB model showed superior accuracy for geometric outputs such as d and b_f, while SVR excelled in predicting f_y. The MAE values across models were consistently low, highlighting the reliability of the predictions. For instance, the MAE for d using HistGB was 0.11 mm, and for f_y using SVR, it was 40.06 MPa, indicating a strong alignment between predicted and actual values.
- Explainability was a key focus of this study, addressed through SHAP analysis. The results revealed that WPB resistance and section height (h) were the most influential features across

all targets, particularly for d and b_f, contributing over 80% of the total feature importance. Meanwhile, features such as h_0 and a_0 showed moderate contributions, depending on the specific output. This detailed explainability ensures transparency in the model's decision-making process, increasing its applicability in safety-critical contexts like structural engineering.

- An important practical contribution of this research is the development of a user-friendly web application that enables immediate design output and accurate predictions. This tool will allow engineers and researchers to input design parameters, especially during iterative early design stages and instantly obtain section and material property predictions. By bridging the gap between research and practical application, the web application facilitates efficient, accessible, and transparent decision-making processes.

The current inverse framework provides a single optimal prediction for each input scenario. While this supports efficient and practical design workflows, we acknowledge that multiple valid solutions may exist for the same performance target. Future work may explore stochastic, multi-output, or uncertainty-aware models to better reflect this design ambiguity.

Lastly, this study highlights the transformative potential of inverse machine learning and explainable AI in structural engineering. By offering a robust, transparent, and efficient methodology, it paves the way for innovative applications in structural design, addressing the challenges of traditional workflows and advancing the field toward data-driven, immediate design solutions.

References

[1] F.P.V. Ferreira, R. Shamass, L.F.P. Santos, V. Limbachiya, K.D. Tsavdaridis, EC3 design of web-post buckling resistance for perforated steel beams with elliptically-based web openings, Thin-Walled Structures 175 (2022) 109196. https://doi.org/10.1016/j.tws.2022.109196.

[2] F.P.V. Ferreira, A. Rossi, C.H. Martins, Lateral-torsional buckling of cellular beams according to the possible updating of EC3, J Constr Steel Res 153 (2019) 222–242. https://doi.org/10.1016/j.jcsr.2018.10.011.

[3] D. Kerdal, D.A. Nethercot, Failure modes for castellated beams, J Constr Steel Res 4 (1984) 295–315. https://doi.org/10.1016/0143-974X(84)90004-X.

[4] F.P.V. Ferreira, C.H. Martins, S. De Nardin, Advances in composite beams with web openings and composite cellular beams, J Constr Steel Res 172 (2020) 106182. https://doi.org/10.1016/j.jcsr.2020.106182.

[5] K.D. Tsavdaridis, C. D'Mello, FE Investigation of Perforated Sections with Standard and Non-Standard Web Opening Configurations and Sizes, in: S.L. Chan (Ed.), 6th International Conference on Advances Is Steel Structures, Hong Kong Institute of Steel Construction, Hong Kong, China, 2009: pp. 213–220. http://www.hkisc.org.

[6] K.D. Tsavdaridis, C. D'Mello, Vierendeel Bending Study of Perforated Steel Beams with Various Novel Web Opening Shapes through Nonlinear Finite-Element Analyses, Journal of Structural Engineering 138 (2012) 1214–1230. https://doi.org/10.1061/(asce)st.1943-541x.0000562.

[7] K.D. Tsavdaridis, C. D'Mello, Optimisation of novel elliptically-based web opening shapes of perforated steel beams, J Constr Steel Res 76 (2012) 39–53. https://doi.org/10.1016/j.jcsr.2012.03.026.

[8] K.D. Tsavdaridis, C. D'Mello, Web buckling study of the behaviour and strength of perforated steel beams with different novel web opening shapes, J Constr Steel Res 67 (2011) 1605–1620. https://doi.org/10.1016/j.jcsr.2011.04.004.

[9] R. Shamass, F.P.V. Ferreira, V. Limbachiya, L.F.P. Santos, K.D. Tsavdaridis, Web-post buckling prediction resistance of steel beams with elliptically-based web openings using Artificial Neural Networks (ANN), Thin-Walled Structures 180 (2022) 109959. https://doi.org/10.1016/j.tws.2022.109959.

[10] F.P.V. Ferreira, R. Shamass, L.F.P. Santos, K.D. Tsavdaridis, V. Limbachiya, Web-post buckling resistance calculation of perforated high-strength steel beams with elliptically-based web openings for EC3, Structures 55 (2023) 245–262. https://doi.org/10.1016/j.istruc.2023.05.139.
[11] M. Rabi, Y.S. Jweihan, I. Abarkan, F.P.V. Ferreira, R. Shamass, V. Limbachiya, K.D. Tsavdaridis, L.F. Pinho Santos, Machine learning-driven web-post buckling resistance prediction for high-strength steel beams with elliptically-based web openings, Results in Engineering 21 (2024) 101749. https://doi.org/10.1016/j.rineng.2024.101749.
[12] M. Ghorbany, S. Ebrahimi-Nejad, M. Mollajafari, Global-guidance chaotic multi-objective particle swarm optimization method for pneumatic suspension handling and ride quality enhancement on the basis of a thermodynamic model of a full vehicle, Proceedings of the Institution of Mechanical Engineers, Part D: Journal of Automobile Engineering 237 (2023) 3334–3352. https://doi.org/10.1177/09544070221148287.
[13] Y. Wang, Z. Han, X. Xu, Y. Luo, Topology optimization of active tensegrity structures, Comput Struct 305 (2024) 107513. https://doi.org/10.1016/j.compstruc.2024.107513.
[14] D. Li, Q. Chen, H. Wang, P. Shen, Z. Li, W. He, Deep learning-based acoustic emission data clustering for crack evaluation of welded joints in field bridges, Autom Constr 165 (2024) 105540. https://doi.org/10.1016/j.autcon.2024.105540.
[15] A. Khosravian, M. Masih-Tehrani, A. Amirkhani, S. Ebrahimi-Nejad, Robust autonomous vehicle control by leveraging multi-stage MPC and quantized CNN in HIL Framework, Appl Soft Comput 162 (2024) 111802. https://doi.org/10.1016/j.asoc.2024.111802.
[16] K. Xu, X. Xiao, L. Wang, M. Lou, F. Wang, C. Li, H. Ren, X. Wang, K. Chang, Data-Driven Materials Research and Development for Functional Coatings, Advanced Science 11 (2024). https://doi.org/10.1002/advs.202405262.
[17] M. Momen, S. Ebrahimi-Nejad, M. Mollajafari, Multi-objective optimization of exponential-cross-section piezoelectric cantilever under tire rotational excitation for self-powered tire pressure monitoring systems, J Clean Prod 500 (2025) 145255. https://doi.org/10.1016/j.jclepro.2025.145255.
[18] H. Chen, B. Huang, H. Zhang, K. Xue, M. Sun, Z. Wu, An efficient Bayesian method with intrusive homotopy surrogate model for stochastic model updating, Computer-Aided Civil and Infrastructure Engineering 39 (2024) 2500–2516. https://doi.org/10.1111/mice.13206.
[19] I. Mascolo, F. Guarracino, S. Sarfarazi, G. Della Corte, A proposal for a simple characterization of stainless steel connections through an equivalent yield strength, Structures 68 (2024) 107043.
[20] S. Sarfarazi, R. Shamass, I. Mascolo, G. Della Corte, F. Guarracino, Some considerations on the behaviour of bolted stainless-steel beam-to-column connections: A simplified analytical approach, Metals 13 (2023) 753. https://doi.org/10.3390/met13040753.
[21] S. Badini, S. Regondi, R. Pugliese, Enhancing mechanical and bioinspired materials through generative AI approaches, Next Materials 6 (2025) 100275. https://doi.org/10.1016/j.nxmate.2024.100275.
[22] F. Masurkar, S. Aggarwal, Z. Wen Tham, L. Zhang, F. Yang, F. Cui, Estimating the elastic constants of orthotropic composites using guided waves and an inverse problem of property estimation, Applied Acoustics 216 (2024) 109750. https://doi.org/10.1016/j.apacoust.2023.109750.
[23] W. Liao, X. Lu, Y. Huang, Z. Zheng, Y. Lin, Automated structural design of shear wall residential buildings using generative adversarial networks, Autom Constr 132 (2021) 103931. https://doi.org/10.1016/j.autcon.2021.103931.
[24] R. Danhaive, C.T. Mueller, Design subspace learning: Structural design space exploration using performance-conditioned generative modeling, Autom Constr 127 (2021) 103664. https://doi.org/10.1016/j.autcon.2021.103664.
[25] A. Teimouri, A. Challapalli, J. Konlan, G. Li, Machine learning assisted design and optimization of plate-lattice structures with superior specific recovery force, Giant 18 (2024) 100282. https://doi.org/10.1016/j.giant.2024.100282.
[26] R.G. McClarren, I.L. Tregillis, T.J. Urbatsch, E.S. Dodd, High-energy density hohlraum design using forward and inverse deep neural networks, Phys Lett A 396 (2021) 127243. https://doi.org/10.1016/j.physleta.2021.127243.
[27] F. Islam, C. Wanigasekara, G. Rajan, A. Swain, B.G. Prusty, An approach for process optimisation of the Automated Fibre Placement (AFP) based thermoplastic composites manufacturing using Machine Learning, photonic sensing and thermo-mechanics modelling, Manuf Lett 32 (2022) 10–14. https://doi.org/10.1016/j.mfglet.2022.01.002.
[28] V.I. Kolesnikov, D.M. Pashkov, O.A. Belyak, A.A. Guda, S.A. Danilchenko, D.S. Manturov, E.S. Novikov, O.V. Kudryakov, S.A. Guda, A.V. Soldatov, I.V. Kolesnikov, Design of double layer protective coatings: Finite element modeling and machine learning approximations, Acta Astronaut 204 (2023) 869–877. https://doi.org/10.1016/j.actaastro.2022.11.007.
[29] A. Challapalli, J. Konlan, G. Li, Inverse machine learning discovered metamaterials with record high recovery stress, Int J Mech Sci 244 (2023) 108029. https://doi.org/10.1016/j.ijmecsci.2022.108029.
[30] D.X.M. Zheng, S.T. Ng, M.M. Kumaraswamy, Applying a Genetic Algorithm-Based Multiobjective Approach for Time-Cost Optimization, J Constr Eng Manag 130 (2004) 168–176. https://doi.org/10.1061/(ASCE)0733-9364(2004)130:2(168).
[31] K.C. SARMA, H. ADELI, Cost optimization of steel structures, Engineering Optimization 32 (2000) 777–802. https://doi.org/10.1080/03052150008941321.

[32] R. Cucuzza, M.M. Rad, M. Domaneschi, G.C. Marano, Sustainable and cost-effective optimal design of steel structures by minimizing cutting trim losses, Autom Constr 167 (2024) 105724. https://doi.org/10.1016/j.autcon.2024.105724.

[33] K.D. Tsavdaridis, C. D'Mello, Structural beam, GB 2492176, 2012.

[34] S. Fares, J. Coulson, D. Dinehart, Design Guide 31: Castellated and Cellular Beam Design, American Institute of Steel Construction, Chicago, IL, USA, 2016.

[35] R. Lawson, S. Hicks, Design of Composite Beams with Large Web Openings SCI P355, Steel Construction Institute, Berkshire, UK, 2011.

[36] N 1993-1-13, Eurocode 3: Design of Steel Structures – Part 1-13: Rules for Beams with Large Web Openings, European Committee for Standardization, Brussels, Belgium, 2024.

[37] Dassault Systèmes Simulia, Abaqus 6.18, (2016).

[38] V. V. Degtyarev, S.J. Hicks, F.P.V. Ferreira, K.D. Tsavdaridis, Design provision assessment for the resistance of laterally restrained cellular steel beams, J Constr Steel Res 226 (2025) 109254. https://doi.org/10.1016/j.jcsr.2024.109254.

[39] P. Panedpojaman, T. Thepchatri, S. Limkatanyu, Novel design equations for shear strength of local web-post buckling in cellular beams, Thin-Walled Structures 76 (2014) 92–104. https://doi.org/10.1016/j.tws.2013.11.007.

[40] R. Shamass, F. Guarracino, Numerical and analytical analyses of high-strength steel cellular beams: A discerning approach, J Constr Steel Res 166 (2020) 105911. https://doi.org/10.1016/j.jcsr.2019.105911.

[41] F.P.V. Ferreira, C.H. Martins, S. De Nardin, Assessment of web post buckling resistance in steel-concrete composite cellular beams, Thin-Walled Structures 158 (2021) 106969. https://doi.org/10.1016/j.tws.2020.106969.

[42] F.P.V. Ferreira, C.H. Martins, S. De Nardin, Sensitivity Analysis of Composite Cellular Beams to Constitutive Material Models and Concrete Fracture, International Journal of Structural Stability and Dynamics 21 (2021) 2150008. https://doi.org/10.1142/S0219455421500085.

[43] F.P.V. Ferreira, R. Shamass, K.D. Tsavdaridis, Database of Finite Element Method Predictions for Web-Post Buckling Resistance of Steel Beams with Elliptically-Based Web Openings, Mendeley Data 1 (2024). https://doi.org/10.17632/wdnyz9jy8k.1.

[44] F. Pedregosa, G. Varoquaux, A. Gramfort, V. Michel, B. Thirion, O. Grisel, M. Blondel, P. Prettenhofer, R. Weiss, V. Dubourg, et al., Scikit-learn: Machine learning in Python, J. Mach. Learn. Res. 12 (2011) 2825–2830.

[45] H.-T. Thai, Machine learning for structural engineering: A state-of-the-art review, Structures 38 (2022) 448–491. https://doi.org/10.1016/j.istruc.2022.02.003.

[46] M. Rabi, I. Abarkan, S. Sarfarazi, F.P.V. Ferreira, A.J. Alkherret, Automated design and optimization of concrete beams reinforced with stainless steel, Struct Concr (2025). https://doi.org/10.1002/suco.202500000

[47] H. Nhat-Duc, T. Van-Duc, Comparison of histogram-based gradient boosting classification machine, random Forest, and deep convolutional neural network for pavement raveling severity classification, Autom Constr 148 (2023) 104767. https://doi.org/10.1016/j.autcon.2023.104767.

[48] Inverse Machine Learning (IML) has been utilise, XGBoost, in: Proceedings of the 22nd ACM SIGKDD International Conference on Knowledge Discovery and Data Mining, ACM, New York, NY, USA, 2016: pp. 785–794. https://doi.org/10.1145/2939672.2939785.

[49] S. Sarfarazi, I. Mascolo, M. Modano, F. Guarracino, Application of artificial intelligence to support design and analysis of steel structures, Metals 15 (2025) 408. https://doi.org/10.3390/met15040408.

[50] S. Zakir Sarothi, K. Sakil Ahmed, N. Imtiaz Khan, A. Ahmed, M.L. Nehdi, Predicting bearing capacity of double shear bolted connections using machine learning, Eng Struct 251 (2022) 113497. https://doi.org/10.1016/j.engstruct.2021.113497.

[51] A. Hoła, S. Czarnecki, Random forest algorithm and support vector machine for nondestructive assessment of mass moisture content of brick walls in historic buildings, Autom Constr 149 (2023) 104793. https://doi.org/10.1016/j.autcon.2023.104793.

[52] S. Sarfarazi, R. Shamass, F. Guarracino, I. Mascolo, M. Modano, Advanced predictive modeling of shear strength in stainless-steel column web panels using explainable AI insights, Results in Engineering 24 (2024) 103454. https://doi.org/10.1016/j.rineng.2024.103454.

[53] V. V. Degtyarev, K.D. Tsavdaridis, Buckling and ultimate load prediction models for perforated steel beams using machine learning algorithms, Journal of Building Engineering 51 (2022) 104316. https://doi.org/10.1016/j.jobe.2022.104316.

[54] M. Rabi, I. Abarkan, R. Shamass, Buckling resistance of hot-finished CHS beam-columns using FE modelling and machine learning, Steel Construction 17 (2024) 93–103. https://doi.org/10.1002/stco.202200036.

[55] I. Abarkan, M. Rabi, F.P.V. Ferreira, R. Shamass, V. Limbachiya, Y.S. Jweihan, L.F. Pinho Santos, Machine learning for optimal design of circular hollow section stainless steel stub columns: A comparative analysis with Eurocode 3 predictions, Eng Appl Artif Intell 132 (2024) 107952. https://doi.org/10.1016/j.engappai.2024.107952.

[56] M. Rabi, F.P.V. Ferreira, I. Abarkan, V. Limbachiya, R. Shamass, Prediction of the cross-sectional capacity of cold-formed CHS using numerical modelling and machine learning, Results in Engineering 17 (2023) 100902. https://doi.org/10.1016/j.rineng.2023.100902.

[57] Y.S. Jweihan, M.J. Al-Kheetan, M. Rabi, Empirical Model for the Retained Stability Index of Asphalt Mixtures Using Hybrid Machine Learning Approach, Applied System Innovation 6 (2023) 93. https://doi.org/10.3390/asi6050093.

[58] M. Rabi, Bond prediction of stainless-steel reinforcement using artificial neural networks, Proceedings of the Institution of Civil Engineers - Construction Materials 177 (2024) 87–97. https://doi.org/10.1680/jcoma.22.00098.

[59] S.M. Lundberg, S.-I. Lee, A unified approach to interpreting model predictions, in: Proceedings of the 31st International Conference on Neural Information Processing Systems, Curran Associates Inc., Red Hook, NY, USA, 2017: pp. 4768–4777.

[60] A. Barredo Arrieta, N. Díaz-Rodríguez, J. Del Ser, A. Bennetot, S. Tabik, A. Barbado, S. Garcia, S. Gil-Lopez, D. Molina, R. Benjamins, R. Chatila, F. Herrera, Explainable Artificial Intelligence (XAI): Concepts, taxonomies, opportunities and challenges toward responsible AI, Information Fusion 58 (2020) 82–115. https://doi.org/10.1016/j.inffus.2019.12.012.

[61] Z. Wang, T. Liu, Z. Long, J. Wang, J. Zhang, Predicting the drift capacity of precast concrete columns using explainable machine learning approach, Eng Struct 282 (2023) 115771. https://doi.org/10.1016/j.engstruct.2023.115771.

[62] W.Z. Taffese, Y. Zhu, G. Chen, Explainable AI based slip prediction of steel-UHPC interface connected by shear studs, Expert Syst Appl 259 (2025) 125293. https://doi.org/10.1016/j.eswa.2024.125293.

[63] H.-A. Le, D.-A. Le, T.-T. Le, H.-P. Le, T.-H. Le, H.-G.T. Hoang, T.-A. Nguyen, An Extreme Gradient Boosting approach to estimate the shear strength of FRP reinforced concrete beams, Structures 45 (2022) 1307–1321. https://doi.org/10.1016/j.istruc.2022.09.112.

[64] S. Wang, J. Liu, Q. Wang, R. Dai, K. Chen, Prediction of non-uniform shrinkage of steel-concrete composite slabs based on explainable ensemble machine learning model, Journal of Building Engineering 88 (2024) 109002. https://doi.org/10.1016/j.jobe.2024.109002.

[65] N. Karathanasopoulos, A. Singh, P. Hadjidoukas, Machine learning-based modelling, feature importance and Shapley additive explanations analysis of variable-stiffness composite beam structures, Structures 62 (2024) 106206. https://doi.org/10.1016/j.istruc.2024.106206.

[66] S. Sarfarazi, R. Shamass, F. Guarracino, I. Mascolo, M. Modano, Exploring the stainless-steel beam-to-column connections response: A hybrid explainable machine learning framework for characterization, Frontiers of Structural and Civil Engineering 19 (2025) 34–59. https://doi.org/10.1007/s11709-025-1162-y.

[67] D. Lai, C. Demartino, Y. Xiao, Interpretable machine-learning models for maximum displacements of RC beams under impact loading predictions, Eng Struct 281 (2023) 115723. https://doi.org/10.1016/j.engstruct.2023.115723.

[68] D. Shahnazaryan, G.J. O'Reilly, Next-generation non-linear and collapse prediction models for short- to long-period systems via machine learning methods, Eng Struct 306 (2024) 117801. https://doi.org/10.1016/j.engstruct.2024.117801.

[69] M. Parvizi, K. Nasserasadi, E. Tafakori, Development of fragility functions of low-rise steel moment frame by artificial neural networks and identifying effective parameters using SHAP theory, Structures 58 (2023) 105315. https://doi.org/10.1016/j.istruc.2023.105315.

[70] E. Junda, C. Málaga-Chuquitaype, K. Chawgien, Interpretable machine learning models for the estimation of seismic drifts in CLT buildings, Journal of Building Engineering 70 (2023) 106365. https://doi.org/10.1016/j.jobe.2023.106365.

[71] S. Zhang, H. Lei, Z. Zhou, G. Wang, B. Qiu, Fatigue life analysis of high-strength bolts based on machine learning method and SHapley Additive exPlanations (SHAP) approach, Structures 51 (2023) 275–287. https://doi.org/10.1016/j.istruc.2023.03.060.

[72] T. Liu, C. Cakiroglu, K. Islam, Z. Wang, M.L. Nehdi, Explainable machine learning model for predicting punching shear strength of FRC flat slabs, Eng Struct 301 (2024) 117276. https://doi.org/10.1016/j.engstruct.2023.117276.

[73] M.T. Ribeiro, S. Singh, C. Guestrin, "Why Should I Trust You?," in: Proceedings of the 22nd ACM SIGKDD International Conference on Knowledge Discovery and Data Mining, ACM, New York, NY, USA, 2016: pp. 1135–1144. https://doi.org/10.1145/2939672.2939778.

[74] B. Kim, E. Glassman, B. Johnson, J. Shah, iBCM: Interactive Bayesian Case Model Empowering Humans via Intuitive Interaction (MIT-CSAIL-TR-2015-010), Technical Report. Massachusetts Institute of Technology (2015) 1–12.

[75] P. Rani, C. Liu, N. Sarkar, E. Vanman, An empirical study of machine learning techniques for affect recognition in human–robot interaction, Pattern Analysis and Applications 9 (2006) 58–69. https://doi.org/10.1007/s10044-006-0025-y.

[76] J. Huysmans, K. Dejaeger, C. Mues, J. Vanthienen, B. Baesens, An empirical evaluation of the comprehensibility of decision table, tree and rule based predictive models, Decis Support Syst 51 (2011) 141–154. https://doi.org/10.1016/j.dss.2010.12.003.
[77] G. James, D. Witten, T. Hastie, R. Tibshirani, An Introduction to Statistical Learning, Springer New York, New York, NY, 2013. https://doi.org/10.1007/978-1-4614-7138-7.
[78] C. Szegedy, W. Zaremba, I. Sutskever, J. Bruna, D. Erhan, Goodfellow Ian, R. Fergus, Intriguing properties of neural networks, ArXiv Preprint (2014).
[79] S. Vakeroudis, M. Yor, Integrability properties and limit theorems for the exit time from a cone of planar Brownian motion, Bernoulli 19 (2013). https://doi.org/10.3150/12-BEJ438.
[80] Y. Zhai, S. Li, X. Zhang, Vibration performance of composite doubly curved shells embedded with damping layer, Int J Struct Stability Dyn 0 (0) 2650265. https://doi.org/10.1142/S0219455426502652.
[81] Y. Su, J. Zhu, X. Long, L. Zhao, C. Chen, C. Liu, Statistical effects of pore features on mechanical properties and fracture behaviors of heterogeneous random porous materials by phase-field modeling, Int J Solids Struct 264 (2023) 112098. https://doi.org/10.1016/j.ijsolstr.2022.112098.
[82] S. Sarfarazi, Steel Beams with Elliptically-Based Web Openings – Interactive App, Streamlit, 2025. Available at: https://steel-beams-with-elliptically-based-web-openings.streamlit.app/ (accessed June 3, 2025).